Eur. Phys. J. A (2016) **52**: 170
DOI 10.1140/epja/i2016-16170-6

THE EUROPEAN PHYSICAL JOURNAL A

Regular Article – Experimental Physics

Neutron capture cross section measurements for ^{238}U in the resonance region at GELINA

H.I. Kim[1,2], C. Paradela[3], I. Sirakov[4], B. Becker[3], R. Capote[5], F. Gunsing[6], G.N. Kim[2], S. Kopecky[3], C. Lampoudis[6], Y.-O. Lee[1], R. Massarczyk[7], A. Moens[3], M. Moxon[8], V.G. Pronyaev[9], P. Schillebeeckx[3,a], and R. Wynants[3]

[1] Korea Atomic Energy Research Institute, Nuclear Data Center, Daejeon 34057, Republic of Korea
[2] Kyungpook National University, Department of Physics, Daegu 41566, Republic of Korea
[3] European Commission, Joint Research Centre, B-2440 Geel, Belgium
[4] Institute for Nuclear Research and Nuclear Energy, BG-1784 Sofia, Bulgaria
[5] International Atomic Energy Agency, Nuclear Data Section, A-1400 Vienna, Austria
[6] CEA-Saclay, Irfu/SPhN, F-91191 Gif-sur-Yvette, France
[7] Los Alamos National Laboratory, Los Alamos, NM 87544, USA
[8] Hyde Copse 3, Marcham, UK
[9] Institute of Physics and Power Engineering, Obninsk, Russia

Received: 15 March 2016 / Revised: 3 May 2016
Published online: 24 June 2016

Communicated by P. Woods

Abstract. Measurements were performed at the time-of-flight facility GELINA to determine the ^{238}U(n, γ) cross section in the resonance region. Experiments were carried out at a 12.5 and 60 m measurement station. The total energy detection principle in combination with the pulse height weighting technique was applied using C_6D_6 liquid scintillators as prompt γ-ray detectors. The energy dependence of the neutron flux was measured with ionisation chambers based on the ^{10}B(n, α) reaction. The data were normalised to the isolated and saturated ^{238}U resonance at 6.67 eV. Special procedures were applied to reduce bias effects due to the weighting function, normalization, dead time and background corrections, and corrections related to the sample properties. The total uncertainty due to the weighting function, normalization, neutron flux and sample characteristics is about 1.5%. Resonance parameters were derived from a simultaneous resonance shape analysis of the GELINA capture data and transmission data obtained previously at a 42 m and 150 m station of ORELA. The parameters of resonances below 500 eV are in good agreement with those resulting from an evaluation that was adopted in the main data libraries. Between 500 eV and 1200 eV a systematic difference in the neutron width is observed. Average capture cross section data were derived from the experimental capture yield in the energy region between 3.5 keV and 90 keV. The results are in good agreement with an evaluated cross section resulting from a least squares fit to experimental data available in the literature prior to this work. The average cross section data derived in this work were parameterised in terms of average resonance parameters and included in a least squares analysis together with other experimental data reported in the literature.

1 Introduction

Cross sections for neutron-induced reactions with ^{238}U as target nucleus are important for a performance assessment and for safety calculations of present and innovative nuclear reactor systems. Due to the role of these cross sections for nuclear energy and criticality safety applications, ^{238}U is one of the key nuclides of the CIELO (Collaborative International Evaluated Library Organization) project [1].

The first evaluation for ^{238}U in the resolved resonance region (RRR) based on a full resonance shape analysis was reported by Moxon *et al.* [2] in 1990. They derived parameters for individual resonances up to 10 keV from a fit to transmission [3, 4], capture [5, 6] and fission cross section data [7], all resulting from measurements at the time-of-flight facility ORELA. The transmission data of Olsen *et al.* [3, 4] resulted from experiments at a 42 m and 150 m station using 7 samples of different areal density (from 0.0002 at/b to 0.175 at/b). The capture data of de Saussure *et al.* [5] and Macklin *et al.* [6] were obtained with a large liquid scintillator installed at a 40 m and 150 m

[a] e-mail: peter.schillebeeckx@ec.europa.eu

station, respectively. The fission widths were derived from the fission areas reported by Difilippo *et al.* [7]. Moxon *et al.* [2] noted that the capture data of both de Saussure *et al.* [5] and Macklin *et al.* [6] were inconsistent with the transmission results of Olsen *et al.* [3, 4]. The data of de Saussure *et al.* [5] above the 6.67 eV resonance were renormalised by a factor of about 0.9. The capture data of Macklin *et al.* [6] required a correction factor of about 1.10 and a background correction equivalent to a cross section of about 0.25 b.

The parameters of Moxon *et al.* [2] are the basis of the evaluation reported by Derrien *et al.* [8] in 2005. Derrien *et al.* [8] extended the upper limit of the RRR from 10 keV to 20 keV by including the transmission data of Harvey *et al.* [9]. The latter resulted from experiments at a 200 m station of ORELA using 3 samples (0.0124 at/b, 0.040 at/b and 0.175 at/b). They also included the energy dependence of the capture cross section in the thermal energy region derived by Corvi and Fioni [10] and transmission measurements with the samples at a temperature of 24 K and 294 K from Meister *et al.* [11]. The experiments of Corvi and Fioni [10] and Meister *et al.* [11] were carried out at GELINA. The spin assignments of Gunsing *et al.* [12] were taken into account. Derrien *et al.* [8] confirmed that the capture data of de Saussure *et al.* [5] and Macklin *et al.* [6] suffered from a bias effect and applied normalization correction factors which were very similar to those of Moxon *et al.* [2]. These corrections are not compatible with the uncertainties quoted by the authors, *i.e.* about 5–10% by de Saussure *et al.* [5] and 8% by Macklin *et al.* [6]. The resonance parameters of Derrien *et al.* [8] together with the thermal capture cross section recommended by Trkov *et al.* [13] were adopted in the main evaluated data libraries. Although for some resonances with an energy ≤ 1.2 keV the neutron widths were changed, the fission widths were not adjusted to be consistent with the fission kernels of Difilippo *et al.* [7], defined by

$$k_f = g\frac{\Gamma_n\Gamma_f}{\Gamma}\,, \tag{1}$$

with g the statistical factor and Γ, Γ_n and Γ_f the total, neutron and fission width, respectively.

In most of the evaluated data libraries the Unresolved Resonance Region (URR) covers the energy region between 20 keV and 150 keV. They refer to the evaluation of Fröhner, which is described in detail in refs. [14, 15]. This evaluation is based on an analysis of experimental data using the Hauser-Feshbach theory with width fluctuations. A similar evaluation was performed by Maslov *et al.* [16] and Courcelle *et al.* [17]. The capture cross section of Fröhner [14, 15], which is strongly based on the data of Kazakov *et al.* [18], is in good agreement with the one of Carlson *et al.* [19]. The latter was derived from a least squares adjustment to experimental data available in the literature using the generalised least squares code GMA developed by Poenitz [20] and named after Gauss, Markov, Aitken. The code is available at the IAEA [21]. The analysis is part of an international cooperative effort to improve cross section standards for neutron-induced reactions organized by the International Atomic Energy Agency [22]. The evaluation process was the result of a simultaneous analysis of various types of experimental data, *i.e.* results of absolute and ratio cross section measurements and spectrum averaged and energy-dependent cross section data. The full data set, which is specified in ref. [23], included: 11 absolute $^{238}\mathrm{U}(\mathrm{n},\gamma)$, 2 shape $^{238}\mathrm{U}(\mathrm{n}\gamma)$, 2 absolute $^{238}\mathrm{U}(\mathrm{n},\gamma)/^{6}\mathrm{Li}(\mathrm{n},\alpha)$ ratio, 5 absolute $^{238}\mathrm{U}(\mathrm{n},\gamma)/^{10}\mathrm{B}(\mathrm{n},\alpha_1)$ ratio, 4 shape $^{238}\mathrm{U}(\mathrm{n},\gamma)/^{10}\mathrm{B}(\mathrm{n},\alpha_1)$ ratio, 4 absolute $^{238}\mathrm{U}(\mathrm{n},\gamma)/^{10}\mathrm{B}(\mathrm{n},\alpha)$ ratio, 9 absolute $^{238}\mathrm{U}(\mathrm{n},\gamma)/^{197}\mathrm{Au}(\mathrm{n},\gamma)$ ratio, 1 shape $^{238}\mathrm{U}(\mathrm{n},\gamma)/^{197}\mathrm{Au}(\mathrm{n},\gamma)$ ratio, 5 absolute $^{238}\mathrm{U}(\mathrm{n},\gamma)/^{235}\mathrm{U}(\mathrm{n},\mathrm{f})$ ratio, 6 shape $^{238}\mathrm{U}(\mathrm{n},\gamma)/^{235}\mathrm{U}(\mathrm{n},\mathrm{f})$ ratio and 1 shape $^{238}\mathrm{U}(\mathrm{n},\gamma)/^{239}\mathrm{Pu}(\mathrm{n},\mathrm{f})$ ratio measurements. The capture cross sections derived by de Saussure *et al.* [5] and Macklin *et al.* [6], which were the only capture data used in the evaluation of Derrien *et al.* [8], strongly deviate from the one of Carlson *et al.* [19] and Fröhner [14,15]. Therefore, they were not included in the evaluation of Fröhner [14,15] and Courcelle *et al.* [17]. A more extended discussion on the status of evaluated data files for ^{238}U in the resonance region is reported by Kopecky *et al.* [24].

The discussion in the previous paragraphs reveals that despite the importance of the $^{238}\mathrm{U}(\mathrm{n},\gamma)$ reaction for nuclear energy applications, no experimental data for this reaction are available in the literature to provide a consistent description of the cross section covering both the RRR and URR. Therefore, the $^{238}\mathrm{U}(\mathrm{n},\gamma)$ cross section in the resonance region is on the Nuclear Data High-Priority Request List [25] with a required uncertainty between 1% and 2%. This request can hardly be fulfilled on the basis of the available experimental data. Also the results of the measurements carried out at the DANCE facility [26] do not solve the problem. The data of Ullman *et al.* [26] have been normalised using the resolved parameters of Derrien *et al.* [8]. Therefore, they do not provide an independent confirmation of the cross section in both the RRR and URR. In addition, differences of more than 10% are observed in the URR between these data and the cross section of Carlson *et al.* [19].

Since the requested accuracy level is difficult to reach from results of a single measurement, complementary experiments at the time-of-flight facilities n_TOF [27,28] and GELINA were proposed within the ANDES project of the of the 7th Framework Programme of the European Commission [29].

In this work results of measurements performed at the time-of-flight facility GELINA of the Joint Research Centre at Geel, Belgium, are presented. To reduce bias effects due to dead time, background, γ-ray attenuation in the sample, shape of the neutron flux, normalization and corrections for self-shielding and multiple interaction events, experiments were carried out at a 12.5 m and 60 m station using samples with different geometry and thickness. An internal normalization procedure based on the well-isolated and saturated 6.67 eV resonance of ^{238}U was applied. Bias effects due to the background were reduced by using permanent background filters [30]. The use of permanent filters improves the accuracy of the data but limits

the energy region that can be analysed. Applying similar procedures in previous measurements the ^{197}Au(n, γ) cross section in the URR was determined with an uncertainty of less than 1.5% [31].

2 Experimental details

2.1 Experimental setup

Experiments were carried out at the neutron time-of-flight (TOF) spectrometer GELINA. A detailed description of this facility can be found in ref. [32]. Intense pulsed electron beams are accelerated, at a repetition rate between 50 Hz and 800 Hz, to a maximum energy of 150 MeV. Electron bunches are compressed to a duration of less than 2 ns by a post-acceleration compression magnet [33]. High-energy electrons generate Bremsstrahlung in a mercury-cooled rotating uranium target [34], where neutrons are produced for about 95% by (γ, n) and 5% by (γ, f) reactions. To produce a neutron spectrum in the low energy region, *i.e.* down to about 10 meV, two water-filled beryllium containers of 4 cm thickness are used as moderators. BF_3 proportional counters, placed at different locations around the target hall, are used to monitor the stability of the accelerator and to normalise TOF spectra to the same total neutron intensity. All measurement stations are equipped with an air-conditioning system to keep the sample at a constant temperature of about 22 °C and to avoid electronic drifts due to temperature changes. In addition, the temperature in the stations is continuously monitored.

The measurements reported in this work were performed at a 12.5 m and 60 m capture measurement station of flight path 5 and 14 of GELINA. These flight paths form an angle of 18° and 9°, respectively, with respect to the normal of the moderator face viewing the flight path. The accelerator was operated at 800 Hz and produced an average beam current of about 55 μA. A shadow bar made of Cu and Pb was placed close to the uranium target to reduce the intensity of both the γ-ray flash and the fast neutron component. The moderated neutron beam at the two stations was collimated to about 75 mm in diameter at the sample position. To minimize the contribution of neutrons from a previous burst ^{10}B overlap filters, with an areal density of about 5×10^{-3} at/b and about 4.2×10^{-2} at/b for the measurements at the 12.5 m and 60 m station, respectively, were placed in the beam. For the measurements at the 12.5 m station a 8 mm thick Pb-filter was used to reduce the intensity of the γ-ray flash. Permanent black resonance filters (Na and/or S) were used to monitor the background during the ^{238}U measurements and reduce bias effects related to background corrections. Due to the use of a Na background filter the data in the energy region between 2.5 keV and 3.5 keV cannot be analysed, while the use of a S filter restricts the analysis of the data to an upper level of 90 keV.

The detection systems (*i.e.* γ-ray detectors, neutron flux detector, electronics and data acquisition system) at the two stations were very similar. Prompt γ-rays originating from a capture reaction were detected by a set of C_6D_6-based liquid scintillators (NE230) of 10 cm diameter and 7.5 cm length. The detection system at the 12.5 m station consisted of 2 detectors and the one at the 60 m station of 4 detectors. Each C_6D_6 detector was positioned at an angle of 125° with respect to the direction of the neutron beam. This geometry reduces systematic effects due to the anisotropy in the primary γ-ray emission which depends on the spin and orbital momentum of the resonance. In section 4.2.2 it is shown that the capture data below 90 keV is dominated by the contribution of *s*- and *p*-wave neutrons, *i.e.* with orbital angular momentum $\ell = 0$ and 1, respectively. For a capture event with $\ell = 0$ and 1 and a spin $J = 1/2$ of the compound nucleus primary γ-rays are emitted isotropically. For *p*-wave neutrons with $J = 3/2$ the impact of anisotropic emission of the primary γ-rays is avoided by placing the detectors at 125° [35].

The detection of neutrons scattered from the sample was reduced by coupling each scintillator to a boron-free quartz windowed EMI9823-KQB photomultiplier (PMT). For each detector the anode signal from the PMT was used to determine the arrival time of the neutron and the signal of the 9th dynode to determine the energy deposited by the γ-ray in the detector.

The total energy detection principle in combination with the pulse height weighting technique [36] was applied to make the detection efficiency for a capture event directly proportional to the total γ-ray energy available in the capture event. The discrimination level of the capture detection system was set to 200 keV deposited energy. This corresponds to the Compton edge of a 330 keV γ-ray. The energy and resolution calibration was based on the response of a 661 keV, 2.6 MeV, 4.4 MeV and 6.1 MeV γ-ray resulting from measurements with Cs, Th, AmBe and PuC radionuclide sources.

In the calculation of the weighting function the γ-rays were supposed to be distributed homogeneously in the sample and the discrimination level of the detection system was taken into account, as discussed in ref. [37]. Due to the relatively low total cross section, the homogeneous distribution of γ-rays is valid in the URR. However, this assumption is not valid for strong resonances in the RRR. Therefore, a procedure proposed in refs. [30,38] and implemented in REFIT [39] was applied. The correction factor to account for the γ-ray and neutron transport in the sample was obtained from Monte Carlo simulations using the MCNP 4C2 code [40] and the prompt γ-ray spectrum in the MCNP 4C2 library. This correction factor is applied on the calculated yield when fitting data in the RRR. The correction factors for the two different sample geometries discussed in sect. 2.2 are compared in fig. 1. Evidently the correction increases with increasing sample thickness. The correction factor in the region of the top of the 6.67 eV resonance is about 1.02 and 1.03 for the thin and thick sample, respectively. An experimental validation of this correction factor as a function of the product of the areal density and total cross section is reported by Borella *et al.* [37] for a 0.1 mm and 1.0 mm thick metallic Au sample (note that in ref. [37] the inverse of F_γ is reported). In addition, Massimi *et al.* [31] demonstrated that applying

Table 1. Characteristics of the ^{238}U, ^{nat}Pb and ^{208}Pb samples used for the capture measurements at GELINA. The masses for the different configurations of ^{238}U samples (denoted by configurations I, II and III) change due to the removal of the oxidation before each measurement campaign. The different sample configurations consisted of two metallic foils, which are denoted by 1 and 2.

Sample	Shape	Area/cm^2	Mass/g	Areal Density/(at/b)	Station	Background filters
^{238}U (1I)	foil	15.94 ± 0.01	6.030 ± 0.015	$(9.570 \pm 0.025) \times 10^{-4}$	12.5 m	S, Na
^{238}U (2I)	foil	16.21 ± 0.01	6.170 ± 0.015	$(9.628 \pm 0.025) \times 10^{-4}$	12.5 m	S, Na
^{238}U (1II)	foil	15.94 ± 0.01	6.009 ± 0.015	$(9.536 \pm 0.025) \times 10^{-4}$	60 m	S
^{238}U (2II)	foil	16.21 ± 0.01	6.134 ± 0.015	$(9.572 \pm 0.025) \times 10^{-4}$	60 m	S
^{238}U (1III)	foil	15.94 ± 0.01	6.000 ± 0.015	$(9.522 \pm 0.025) \times 10^{-4}$	12.5 m	Na
^{238}U (2III)	foil	16.21 ± 0.01	6.112 ± 0.015	$(9.537 \pm 0.025) \times 10^{-4}$	12.5 m	Na
^{nat}Pb (1)	foil	15.89 ± 0.01	9.264 ± 0.001	$(1.694 \pm 0.001) \times 10^{-3}$		
^{nat}Pb (2)	foil	16.23 ± 0.01	9.442 ± 0.001	$(1.691 \pm 0.001) \times 10^{-3}$		
^{208}Pb	disc	50.27 ± 0.02	29.732 ± 0.001	$(1.713 \pm 0.001) \times 10^{-3}$		

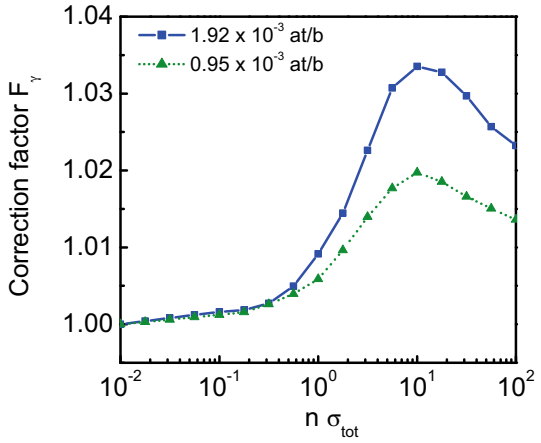

Fig. 1. Correction factor F_γ to account for the γ-ray and neutron transport in the sample. The factor is plotted as a function of the product of the areal number density n and total cross section σ_{tot}. The characteristics of the two different geometries are specified in table 1.

the procedure proposed in refs. [30,38] the normalization factors for measurements with a 0.01 mm, 0.52 mm and 1.00 mm thick Au sample based on the 4.9 eV resonance differ by less than 1%.

The shape of the neutron spectrum was measured in parallel with ^{10}B Frisch gridded ionisation chambers placed at about 80 cm before the sample. They were operated with a continuous flow of a mixture of argon (90%) and methane (10%) at atmospheric pressure. At the 12.5 m station a double chamber was used with a common cathode loaded with two layers of ^{10}B. The ^{10}B layers, with an effective diameter of about 84 mm and areal number density of about 2.1 10^{-6} at/b, were evaporated back-to-back on a 30 μm thick aluminium backing and the entrance and exit windows of the chamber had a thickness of 40 μm. The chamber installed at the 60 m station consisted of three back-to-back layers of ^{10}B with a total areal number density of 1.3×10^{-5} at/b ^{10}B. The impact of kinematic effects for the flux measurements was strongly reduced by using multiple chambers with a common cathode loaded with two layers of ^{10}B. Such a back-to-back configuration together with an energy threshold on the amplitude spectrum accepting the signals from both the ^{7}Li and α particles strongly reduces a possible bias related to the forward-to-backward emission ratio [41].

The TOF of a neutron was determined by the time difference between the stop signal either from the ^{10}B-chamber or from the C_6D_6 detectors and the start signal, given at each electron burst. The TOF was determined with a multi-hit fast time coder with a 1.0 ns resolution. The TOF and the pulse height of detected events were recorded in list mode using a data acquisition system developed at the IRMM [42]. The stability of the two detection systems and the accelerator operating conditions (*i.e.* frequency, current and neutron output) were verified in cycles of 900 seconds. Only cycles with a 800 Hz operating frequency and for which the total neutron intensity and response of the detection systems deviated by $\leq 3\%$ from the average were selected. The stability of the C_6D_6 detectors was monitored on a weekly basis by measurements of the 2.6 MeV γ-ray from the ^{232}Th decay chain.

Each detection system produced a veto signal that created a fixed dead time as soon as an event was detected. The fixed dead time of the capture and neutron detection chains were derived from registering the time-interval between successive events. For the flux measurements the dead time was 3500 ns, with a maximum dead time correction $\leq 1\%$. The dead time for the capture measurement systems was 2800 ns. Only data for which the dead time correction was $\leq 20\%$ were analysed. Possible bias effects due to such corrections are very small as was demonstrated in refs. [30,43]. However, it limits the upper energy region of the data obtained at the 12 m station to ≤ 70 keV for measurements without the sulfur permanent filter. The presence of the sulfur filter strongly reduces the impact of the γ-ray flash and its contribution to the dead time correction.

2.2 Samples

Capture cross section data for ^{238}U were derived from results of measurements using metallic uranium samples. Their characteristics are summarized in table 1. Two

metallic samples, denoted by (1) and (2) in table 1, were used. They originated from the same batch of uranium material which was enriched to 99.99% in ^{238}U. The isotopic composition of this batch was verified by mass spectrometry in 1984 and resulted in: $^{234}\mathrm{U} < 1\,\mathrm{ppm}$, $^{235}\mathrm{U} < 11\,\mathrm{ppm}$ and $^{236}\mathrm{U} < 1\,\mathrm{ppm}$. The areal density of the two samples was derived from a measurement of the mass and the area. The area was determined by an optical surface inspection with a microscopic based measurement system from Mitutoyo (Quick-Scope QS200Z) [44]. The mass of the sample was determined before and after each measurement campaign. Before and after each measurement the surface of each sample was cleaned with cleanroom wipes and methanol to remove possible oxidation layers. This explains the differences in mass values in table 1. A conservative uncertainty on the areal density of about 0.25% was used for the analysis.

Measurements with two different sample geometries (configuration I and configurations II, III in table 1) and different permanent background filters were carried out. For all ^{238}U and ^{nat}Pb sample geometries the area of the neutron beam at the sample position ($\sim 38\,\mathrm{cm}^2$) was larger than the effective sample area. The use of different samples reduces systematic effects related to background corrections and to the sample geometry and thickness, *i.e.* correction factor F_γ (see sect. 2.1) and corrections for self-shielding and multiple interaction F_c (see sect. 4.2.1). During a first campaign at 12.5 m the two ^{238}U samples were placed in a back-to-back geometry resulting in a 12.2 g sample with nominal dimensions ($54\,\mathrm{mm}\times 30\,\mathrm{mm}\times 0.46\,\mathrm{mm}$) and an areal number density of $(1.920 \pm 0.005) \times 10^{-3}$ at/b. The measurements with this sample geometry, denoted by configuration I in table 1, were carried out with permanent Na and S filters in the beam to monitor the background level at about 2.85 keV and 102 keV, respectively. In a second campaign at 12.5 m the two samples were combined to form a 12.1 g sample with nominal dimensions ($53\,\mathrm{mm} \times 60\,\mathrm{mm} \times 0.23\,\mathrm{mm}$) and an areal number density of $(0.9530 \pm 0.0025) \times 10^{-3}$ at/b (configuration III in table 1). During these measurements only the Na filter was used as permanent background filter. A similar sample geometry was used for the measurements at the 60 m station (configuration II in table 1). For these measurements the areal number density of the ^{238}U sample was $(9.554 \pm 0.025) \times 10^{-4}$ at/b and only the S filter was used as a permanent background filter.

3 Data reduction

The experimental yield Y_{exp} was deduced from the ratio of the TOF response of the capture detection system and the one of the neutron flux detector by [30]:

$$Y_{exp} = \frac{N_c}{S_n + E_n \frac{m_U}{m_n + m_U}} \frac{C_w - B_w}{C_\varphi - B_\varphi} \frac{Y_\varphi}{T_\varphi}\,, \qquad (2)$$

where E_n is the kinetic energy of the neutron and S_n is the neutron separation energy. The atomic mass of the neutron and ^{238}U target nucleus are denoted by m_n and m_U, respectively. The dead-time corrected weighted C_6D_6 response is denoted by C_w and the dead-time corrected response of the flux detector by C_φ. Their corresponding background contributions are B_w and B_φ, respectively. The TOF spectra in eq. (2) were normalised to the same neutron beam intensity using the total counts of the ^{10}B ioinisation chamber.

The ratio of the reaction yield of the boron chamber Y_φ and the attenuation of the flux in the chamber T_φ, dependent equivalently on TOF or energy, is given by:

$$\frac{Y_\varphi}{T_\varphi} = e^{n_\varphi \sigma_{tot}} \left(1 - e^{-n_\varphi \sigma_{tot}}\right) \frac{\sigma_\alpha}{\sigma_{tot}}\,, \qquad (3)$$

where n_φ is the total areal number density of the ^{10}B layers in the ionisation chamber, σ_α the cross section for the $^{10}\mathrm{B}(\mathrm{n},\alpha)$ reaction and σ_{tot} the total cross section for neutron-induced reactions in ^{10}B. Before applying eq. (2) a transformation of variables was applied to account for the $\sim 80\,\mathrm{cm}$ difference in the position of the ionisation chamber and the capture sample. The normalization factor N_c in eq. (2) accounts for energy-independent factors such as *e.g.* the absolute neutron flux, the effective sample area seen by the neutron beam, the efficiency of the flux detector and the solid angle subtended by the sample and the C_6D_6 detectors.

3.1 Background correction for flux measurements

The background contribution for the flux measurements was approximated by an analytical expression applying the black resonance technique. The analytical function was a sum of a time-independent and two time-dependent components:

$$B_\varphi(t) = k_\varphi \left(a_0 + a_1 e^{-\lambda_1 t} + a_2 e^{-\lambda_2 (t+\tau_0)}\right), \qquad (4)$$

where t denotes the TOF of the detected event. The analytical expression and decay constants λ_1 and λ_2 were determined from additional measurements with Ag, W, Co, Na, and S black resonance filters and measurements at a lower operating frequency. The time-independent component a_0 accounts for ambient background and scattered neutrons which are produced in the target room but which have completely lost their time correlation with the pulsed electron beam. The first time-dependent component is mainly due to neutrons that are scattered inside the measurement station and from neutrons scattered at other flight paths. Its amplitude was adjusted to a resonance dip resulting from the presence of a permanent black resonance filter. The second time-dependent component corresponds to the contribution due to overlap neutrons, *i.e.* slow neutrons from previous accelerator pulses. This contribution was estimated by an extrapolation of the TOF spectrum at the end of the cycle. It is approximated by an exponential decay, where the parameter τ_0 is equal to the spacing between the electron bursts. For a 800 Hz operating frequency $\tau_0 = 1.25\,\mathrm{ms}$. The response of the ionisation chamber and the estimated background contribution for

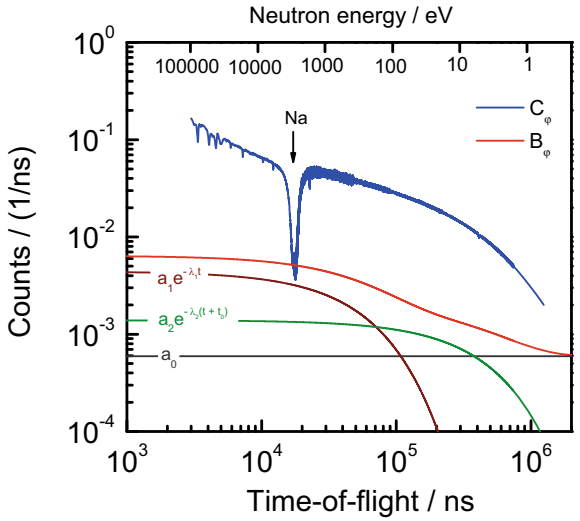

Fig. 2. Time-of-flight spectra obtained with the ^{10}B loaded ionisation chamber. The spectrum (C_φ) is compared with the total background (B_φ) and its contribution (see eq. (4)). The spectra are related to the experiments at 12.5 m and sample configuration III (see table 1). The dip due to the 2.8 keV resonance of Na is indicated.

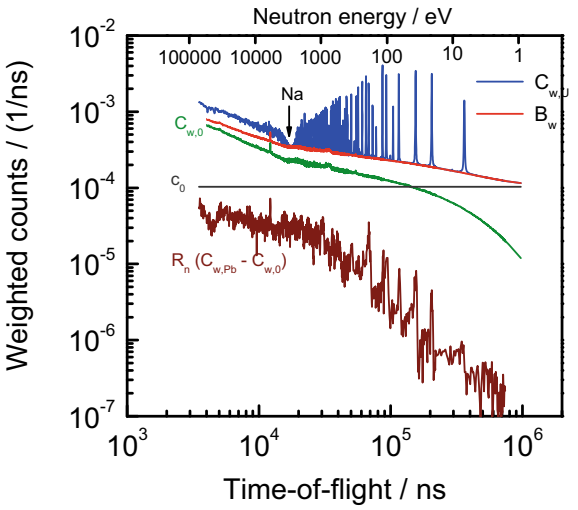

Fig. 3. Weighted time-of-flight spectra obtained with the C_6D_6 detectors. The spectrum for the ^{238}U sample $C_{w,U}$ is compared with the total background B_w and its contributions (see eq. (5)). The spectra are related to the experiments at 12.5 m and sample configuration III (see table 1). The dip due to the 2.8 keV resonance of Na is indicated.

the ^{238}U(n, γ) measurements at 12.5 m with sample configuration III are compared in fig. 2.

The parameter $k_\varphi = 1.00 \pm 0.03$ is introduced in eq. (4) to account for uncertainties due to systematic effects in the background correction. This parameter, which is valid for the measurements at 12.5 m and 60 m, was obtained from results of a series of additional measurements with Ag, W, Co, Na and S black resonance filters in the beam (separately and combined). The parameter together with its uncertainty was derived from a statistical analysis of the difference between observed black resonance dips and the background estimated by the analytical expression in eq. (4).

3.2 Background correction for the C_6D_6 response

The total background contribution to the weighted response of the C_6D_6 detectors was expressed as:

$$B_w(t) = k_\gamma[b_0 + C_{w,0}(t) + R_n(t)(C_{w,Pb}(t) - C_{w,0}(t))], \quad (5)$$

where b_0 is a time-independent contribution, $C_{w,0}$ and $C_{w,Pb}$ are the weighted counts from measurements with no sample and with an almost purely scattering ^{208}Pb sample, respectively. The weighted spectra $C_{w,0}$ and $C_{w,Pb}$ were derived with the weighting function for the U sample. They were normalised to the same integrated neutron intensity and corrected for the time-independent background. To account for the different geometry of the ^{238}U and ^{208}Pb samples (see table 1), the ^{208}Pb spectra were normalised to the ^{nat}Pb spectra in regions where no resonance contributions from ^{204,206,207}Pb were observed. The correction factor R_n is the ratio of the neutron scattering yield of the U and Pb sample. This factor, which is expressed as a function of TOF, was derived from Monte Carlo simulations using the MCNP 4C2 code. The weighted response for measurements at the 12.5 m station with sample configuration III and the different background contributions are compared in fig. 3.

The factor $k_\gamma = 1.00 \pm 0.03$, which is introduced to account for uncertainties due to systematic effects in the background correction, was obtained from a systematic study of the background based on eq. (5) and the background dips present in the TOF spectra due to the presence of black resonance filters. In this study results of previous capture cross section measurements at GELINA under similar conditions (*e.g.*, refs. [31,45]) were included.

The contribution of prompt fission γ-rays from ^{238}U (n,f) to the weighted response was estimated using a prompt γ-ray spectrum for ^{238}U(n,f) of Litaize *et al.* [46] and an average total prompt γ-ray energy of 6.7 $\pm$ 0.5 MeV [47, 48]. The prompt fission and capture γ-ray spectra were supposed to be independent of incoming neutron energy. The ratio of the weighted detection efficiency for a fission event and capture event was estimated to be 0.6 ± 0.3. Due to the low contribution of this background component, a conservative estimate of the relative uncertainty of this ratio is the relative standard deviation of the total prompt fission γ-ray energy distribution. This standard deviation is about 3.5 MeV [49]. For the 726 eV resonance, for which the largest fission to capture ratio is reported [7], the relative contribution due to prompt fission γ-rays is $\leq 5\%$. In the other energy regions of interest the contribution is $\leq 0.5\%$. The background contribution due to prompt fission γ-rays was included in the resonance shape analysis using 0.6 for the detection efficiency of a fission event relative to a capture event.

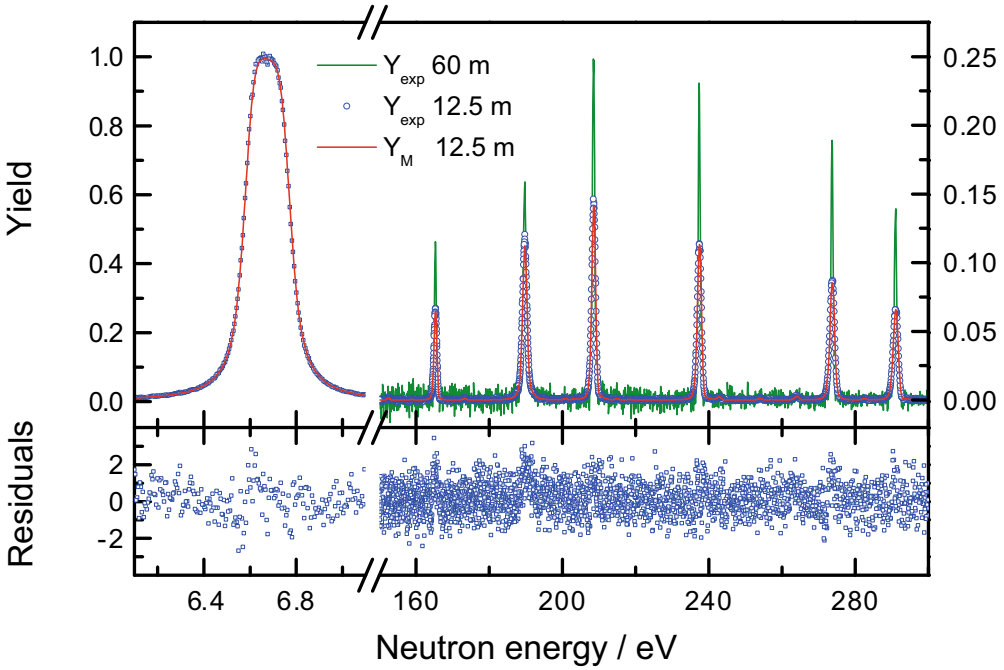

Fig. 4. Capture yield Y_{exp} obtained from measurements at 12.5 m and 60 m using the sample configuration III and II, respectively, with the same geometry. The theoretical yield Y_M for the 12.5 m data resulting together with the corresponding residual are also shown. The theoretical yield and residual for the 60 m data are shown in fig. 6.

3.3 Normalisation

The experimental yields resulting from the measurements at 12.5 m obtained with the two sample geometries (I and III) were internally normalised using the profile of the well-isolated and saturated resonance at 6.67 eV. This resonance has a low scattering to capture ratio of about 0.06. The normalisation was obtained by a least squares adjustment of the experimental yield with only the normalization factor as a free fitting parameter. Only data points close to the resonance top, with a yield ≥ 0.75, were considered in the fit. Using a saturated profile from a resonance with a neutron width that is much smaller than the radiation width results in a normalisation that is nearly independent of the resonance parameters and sample thickness, as demonstrated in refs. [30, 45, 50, 51]. If, in addition, an internal normalization is applied most of the experimental conditions remain unchanged and a bias due to systematic effects, such as variations of detector and accelerator operating conditions, effective sample area seen by the neutron beam, solid angle between sample and detector, is nearly eliminated [30]. The normalisation factor for the capture data obtained at 60 m was derived from a simultaneous resonance shape analysis including the 12.5 m capture data and the transmission data of Olsen *et al.* [3, 4]. Only data in the energy region between 150 eV and 300 eV were included in this analysis. The result of such an analysis is shown in fig. 4. The experimental yield obtained from the 12.5 m and 60 m measurements obtained with the same sample geometry are plotted together with the yield calculated for the 12.5 m data. The difference in peak height between the 12.5 m and 60 m data is due to a difference in resolution. The residuals in the figure are defined by

$$\frac{Z_{exp} - Z_M}{u_{Z_{exp}}}, \tag{6}$$

where Z_{exp} and Z_M are the experimental and theoretical observable, respectively, and $u_{Z_{exp}}$ is the uncorrelated uncertainty of Z_{exp} only due to counting statistics.

The normalisation factor derived from such an analysis differed by less than 1% from the value derived from a combined analysis of only the 12.5 m and 60 m capture data obtained with the same sample geometry. Using a sample with the same geometry the normalisation factor can be obtained by analysing areas of isolated resonances. Such an area analysis is almost insensitive to the resonance parameters.

As noted in refs. [30, 31, 37, 45] the influence of systematic effects depending on the specific character of the γ-ray cascade are largely reduced when the γ-ray emission spectrum for the resonance normalisation is similar to the one for the energy region under investigation. To verify the impact of a difference in prompt γ-ray emission spectrum, the C_6D_6 amplitude spectra of the 6.67 eV resonance and the one for capture events between 5 keV and 70 keV were compared. The comparison in fig. 5 reveals a difference between these spectra, which is most probably due to a difference in γ-ray spectrum for s- and p-wave neutrons. In the region between 5 keV and 70 keV the (n, γ) events are dominated by p-wave neutrons (see sect. 4.2.3). Hence, a bias due to a different influence of the 200 keV discrimination level for s-wave and p-wave neutrons cannot be

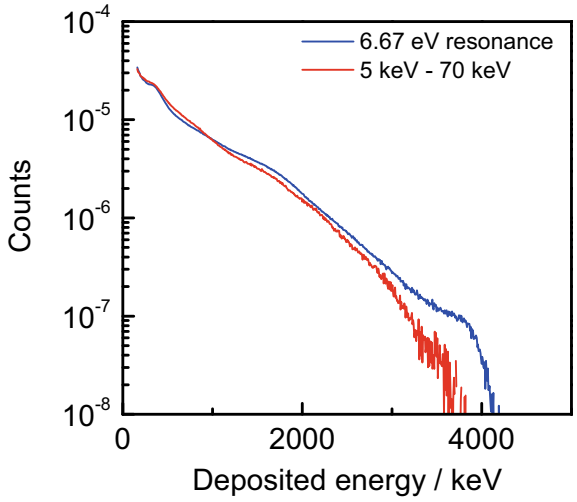

Fig. 5. Spectrum of the energy deposited in the C_6D_6 detector for events with an energy close to the 6.67 eV s-wave resonance and events with a neutron energy between 5 keV and 70 keV. The observed spectra have been corrected for their background contributions.

excluded. To quantify a possible bias, a procedure similar to the one in ref. [31] was applied.

The statistical code γDEX [52,53] was used to simulate γ-ray spectra from capture states with different spin and parity. In the calculations the level scheme of ^{239}U below 1500 keV was taken from the ENSDF data base [54]. For the level density in the continuum, a constant temperature model was assumed with $kT = (320 \pm 20)$ keV and an average resonance spacing $D_0 = (20.8 \pm 0.3)$ eV at zero energy [55]. The $E1$ γ-ray strength was approximated by a triaxial Lorentzian description [56]. For the $M1$ γ-strength a parameterization proposed by Hyde *et al.* [57] resulting from an adjustment to experimental data was used. For $E2$ transitions the recommendation of the RIPL-3 data base [58] was followed.

The γ spectra obtained with γDEX were used to estimate the contribution of transitions with an energy below 330 keV for (n, γ) events induced by s- and p-wave neutrons. The total contribution of transitions with an energy ≤ 330 keV is 15.4% and 14.7% for s- and p-wave neutrons, respectively. When weighting the intensities with the transition energies the relative missing contribution reduces to 1.62% and 1.56%, respectively. Hence, a bias due to the threshold and difference in γ-ray spectrum is expected to be very small.

The impact of a difference in γ-ray transition spectra can also be assessed by comparing the capture yields obtained from the weighted and not weighted response of the C_6D_6 detectors [45]. Therefore, the yields derived from the not weighted and weighted response obtained from the 60 m data were calculated by repeating the complete data reduction procedure including background subtraction and normalization. In the region between 5 keV and 90 keV the average ratio of the yields derived from the non-weighted and weighted data is about 0.99 and does not show a strong dependence on the neutron energy.

Finally, a 1.5% uncertainty was assigned on the normalization factor. This uncertainty, which includes the uncertainty to determine the shape of the neutron flux and the uncertainty of the areal density, was evaluated from a statistical analysis of N_c values obtained from fits in different regions and using resonance parameters that were varied by 5%. For the saturated resonance at 6.67 eV, fit regions were varied with the minimum observed yield ranging from 0.75 to 0.95. This result confirms results of similar systematic studies on the normalisation of capture data obtained at GELINA in refs. [31,37,45].

3.4 Time-of-flight to energy conversion

The zero point of the time scale for the capture detection system was deduced from the position of the γ-ray flash with an accuracy better than 1 ns. A resonance shape analysis of ^{238}U(n, γ) resonances below 500 eV was used to define the effective flight path length using the resonance energies of Derrien *et al.* [8]. The flight path lengths were (12.942 ± 0.002) m and (12.964 ± 0.002) m for the measurements with the (1.92×10^{-3}) at/b and (0.953×10^{-4}) at/b samples, respectively. For the measurements with sample configuration II the flight path length was (58.580 ± 0.005) m. The quoted uncertainties are only due to the propagation of counting statistics uncertainties and do not account for uncertainties on the resonance energies.

The zero point of the time scale for the flux system was derived from dips in the TOF spectrum due to Pb resonances. The flight path length was derived from resonance dips in the TOF spectra obtained from measurements with the W and Ag filters in the beam.

3.5 Covariance data

The AGS (Analysis of Geel Spectra) package [59,60] was used to derive the experimental yield from TOF histograms. This package includes all basic spectrum operations and performs a full uncertainty propagation accounting for both correlated and uncorrelated uncertainty components starting from uncorrelated uncertainties due to counting statistics of the TOF spectra. The AGS formalism, which results in a substantial reduction of space for data storage, is recommended by the International Nuclear Data Committee (INDC) to store experimental data in the EXFOR data base [61,62].

Applying the AGS concept the covariance matrix $\mathsf{V}_{Z_{exp}}$ of an experimental observable Z_{exp} is given by

$$\mathsf{V}_{Z_{exp}} = \mathsf{U}_u + \mathsf{S}(\boldsymbol{\eta})\mathsf{S}^T(\boldsymbol{\eta}), \tag{7}$$

where U_u is a diagonal matrix containing the contribution of all uncorrelated uncertainty components and $\mathsf{S}(\boldsymbol{\eta})$ is a matrix representing the contribution of components creating a correlated contribution, *e.g.* $\boldsymbol{\eta} = \{k_\varphi, k_\gamma, N_c\}$. The data in the matrix $\mathsf{S}(\boldsymbol{\eta})$ can be used to reconstruct the full covariance matrix and to verify separately the impact of different uncertainty components [60].

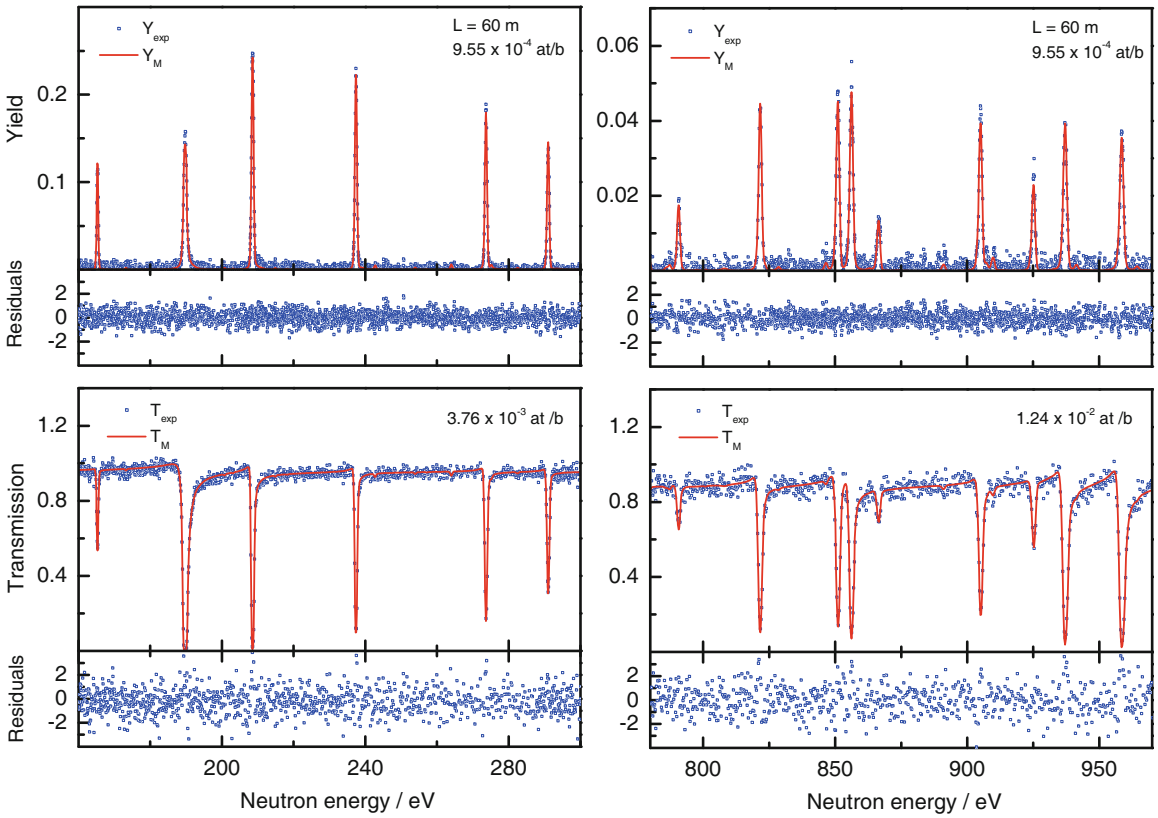

Fig. 6. Comparison of experimental and theoretical observables. The experimental yield Y_{exp} obtained at 60 m with sample II is compared with the theoretical yield Y_M. The experimental transmission T_{exp} from measurements with a 3.76×10^{-3} and 1.24×10^{-3} at/b sample at ORELA is compared with the theoretical transmission T_M. The calculated observables were obtained from calculations with REFIT after adjusting the parameters to the experimental data as described in the text. The residuals are calculated according to eq. (6) considering only the uncorrelated uncertainties due to counting statistics.

4 Results

4.1 Energy region below 1200 eV

The resonance shape analysis code REFIT [39] was used to determine resonance parameters by adjusting them in a least squares fit to the experimental yields obtained in this work and the transmission data of Olsen *et al.* [3,4]. This code, which is based on the Reich-Moore [63] approximation of the R-matrix formalism [64], accounts for various experimental effects such as Doppler broadening, neutron self-shielding, multiple interaction events and the response function of the TOF-spectrometer [30]. To account for the impact of the neutron flux and γ-ray attenuation in the sample, discussed in sect. 2.1, the procedure proposed in refs. [30,38] was implemented in REFIT.

The initial resonance parameters, including parity and spin, and effective scattering radius $R = 9.48$ fm were taken from ENDF/B-VII.1. The free gas model, with the effective temperature $T_{eff} = 300$ K used by Derrien *et al.* [8], was applied to account for the Doppler effect. The response functions of GELINA were obtained from Monte Carlo simulations [65,66] and introduced numerically. For the analysis of the transmission data of Olsen *et al.* [3,4] the time response of the detector and the ORELA TOF-spectrometer were approximated by analytical models implemented in REFIT. The response of the ORELA TOF-spectrometer was derived by Moxon [67]. This response resulted from a systematic study of various transmission, capture and fission cross section data obtained at ORELA.

As mentioned in sect. 3.3, the 12.5 m capture data were normalised based on an analysis of the 6.67 eV saturated resonance and the normalization factor for the 60 m capture data was derived from an analysis of the data between 150 eV and 300 eV.

The 12.5 m and 60 m capture data were analysed starting at an energy of about 3 eV and 150 eV, respectively. These lower limites are due to the reduction of the neutron flux by the overlap filters. The lower limit of the transmission data was 0.5 eV. Parameters were derived for resonances with an energy ≤ 1200 eV. The upper limit is mainly due to the limited resolving power of the 12.5 m capture data and to limited counting statistics of the 60 m data above 1200 eV.

The data were fitted in separate regions with a maximum width of 50 eV or including a maximum of 10 resonances. Up to 1200 eV the capture and transmission data could be parameterised by using one set of resonance parameters, without applying any additional background and normalization corrections. This means that in this region the capture data are fully consistent with

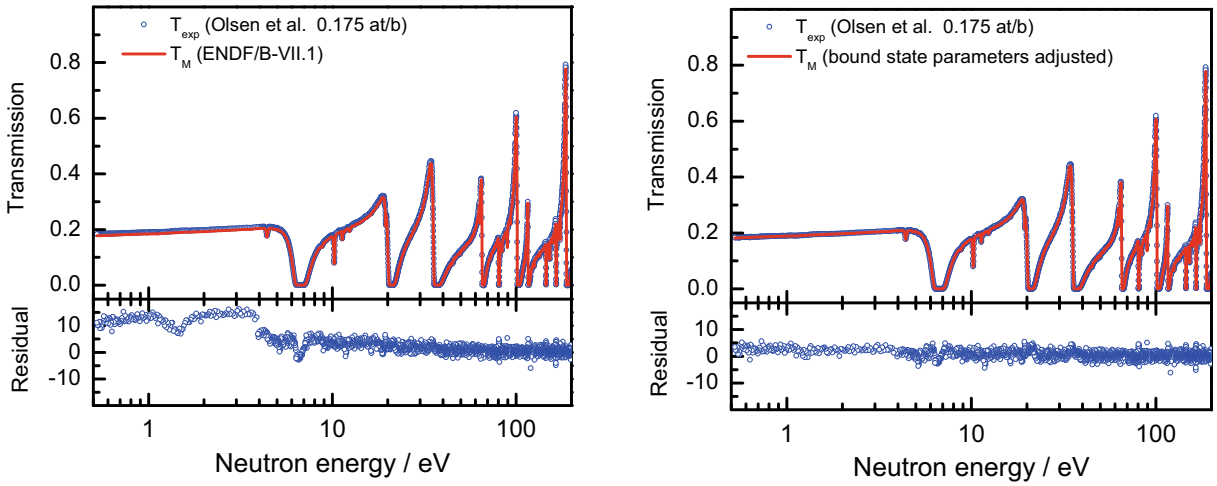

Fig. 7. Comparison of the experimental T_{exp} and theoretical transmission T_M. The experimental data result from measurements at ORELA with a thick ^{238}U sample (areal number density of 0.175 at/b). The theoretical transmission results from calculations with REFIT using the ENDF/B-VII.1 resonance parameters (left) and a file based on the ENDF/B-VII.1 parameters with only the parameters of two bound states (*i.e.* those of −7 eV and −33 eV in ENDF/B-VII.1) adjusted (right). The residuals are calculated according to eq. (6) considering only the uncorrelated uncertainties due to counting statistics.

the transmission data. Examples of the result of a simultaneous fit to the capture and transmission data are shown in fig. 6 and fig. 7. For all fits a $\chi^2/\nu \leq 1.2$ was obtained considering only the uncorrelated uncertainties due to counting statistics. The reduced chi-square and the residuals (see eq. (6)) reveal that the experimental data are consistent with the theoretical calculation within the uncorrelated uncertainties due to counding statistics. In some cases the experimental data, in particular the capture data at 12.5 m, were not fully reproduced. This is due to limitations of the response functions and/or corrections for multiple interaction events in case of capture data. By combining results of capture and transmission data derived from measurements with different samples at different distances and installations the impact of these effects is reduced.

To fit the transmission data of Olsen *et al.* [3,4] without applying a normalization factor, the contribution of the bound states had to be adjusted. This is illustrated in fig. 7, which compares the experimental T_{exp} and theoretical transmission T_M for the uranium sample with a 0.175 at/b areal density. Using the parameters of ENDF/B-VII.1, which are adopted from Derrien *et al.* [8], the theoretical and experimental transmission are not consistent. This suggests that Derrien *et al.* [8] applied a normalization correction to the experimental transmission to get a consistent fit. Figure 7 reveals that a good agreement between T_{exp} and T_M can also be obtained by adjusting the parameters of bound states without applying any correction on the experimental data. The resonance energies and neutron widhts of two bound states, *i.e.* the −7 eV and −33 eV resonances in the ENDF/B-VII.1 file, were adjusted maintaining the thermal capture cross section of (2.683±0.012) b recommended by Trkov *et al.* [13] and the energy dependence of the capture cross section between 0.002 eV and 0.1 eV reported by Corvi and Fioni [10]. After this adjustment the elastic scattering cross section at thermal energy was reduced by about 0.5% compared to the one in ENDF/B-VII.1. The corresponding coherent scattering length $b_c = (8.57 \pm 0.02)$ fm is in agreement with the one $b_c = (8.63 \pm 0.04)$ fm determined by Koester *et al.* [68]. The capture data were not sensitive to the change in parameters of the bound states.

The final parameters, *i.e.* resonance energy E_r, spin and parity J^π, neutron width multiplied with the statistical factor $g\Gamma_n$ and radiation width Γ_γ are listed in table 5 in appendix A. The quoted uncertainties result from a propagation of only uncorrelated uncertainties due to counting statistics. The production of covariance data accounting for all uncertainty components is in progress. For some resonances both Γ_n and Γ_γ were derived. For these resonances the correlation coefficients $\rho(\Gamma_n, \Gamma_\gamma)$ are given. They also result from propagating only the uncorrelated uncertainties to counting statistics. The assignment of orbital angular momentum ($\ell = 0$ or 1) was based on the approach proposed by Bollinger and Thomas [69]. An upper level $g\Gamma_n^1 \leq 45$ meV was defined for the reduced resonance strength of p-wave resonances, as illustrated in fig. 8. Applying this criterion, the assignment in ENDF/B-VII.1 for the resonances at $E_r = 488.85$ eV, 721.56 eV and 730.02 eV was changed from $\ell = 0$ to $\ell = 1$.

From the data in appendix A an average radiation width $\langle\Gamma_\gamma\rangle = 22.5$ meV was derived with a variation of 1 meV at one standard deviation. This value was taken considering the weighted (22.6 meV) and unweighted (22.4 meV) average radiation width derived from the data with a correlation coefficient $\rho(\Gamma_n, \Gamma_\gamma) \leq |0.75|$. The average radiation width was adopted in case the data was not sensitive to the radiation width, including the resonance at 721.56 eV for which a $\Gamma_\gamma = 3.15$ meV is recommended in ENDF/B-VII.1. The χ^2/ν for the fit in the region of this resonance was significantly better using a

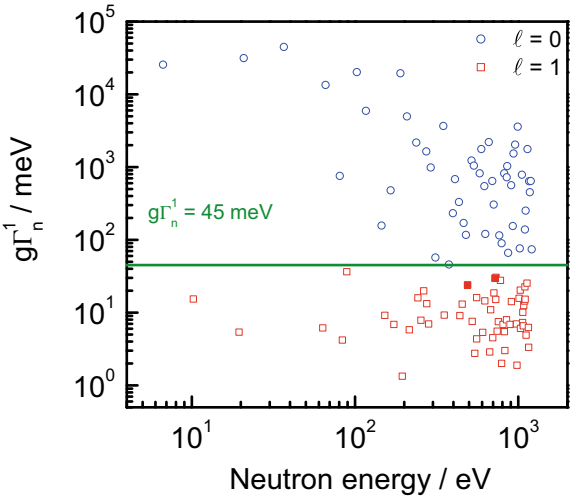

Fig. 8. Reduced neutron strength $g\Gamma_n^1$ as a function of the neutron energy supposing that all resonances have $\ell = 1$. The selection $\ell = 0$ or 1 is based on an upper level $g\Gamma_n^1 \leq 45$ meV for $\ell = 1$. The resonances for which the ℓ-assignment was changed are indicated with a full symbol.

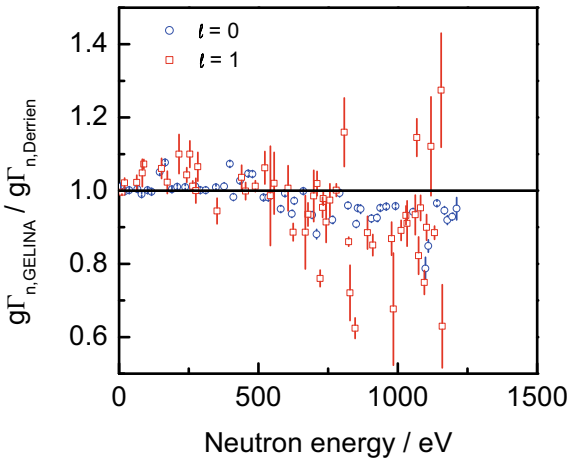

Fig. 9. Ratio of the neutron widths obtained in this work and those derived by Derrien *et al.* [8] as a function of the neutron energy.

$\Gamma_\gamma = 22.5$ meV. The fission widths were adjusted to reproduce the fission areas of Difilippo *et al.* [7]. These widths are also included in appendix A.

The average radiation width is about 2.2% smaller compared to the one derived by Derrien *et al.* [8]. The average radiation width $\langle\Gamma_\gamma\rangle = (24 \pm 2)$ meV derived from the γDEX calculations in sect. 3.3 is consistent with $\langle\Gamma_\gamma\rangle = 22.5$ meV. The ratio of the neutron strength $g\Gamma_n$ obtained in this work and those derived by Derrien *et al.* [8] is shown as a function of the neutron energy in fig. 9. Below 500 eV the weighted average ratio is 1.004 with a standard variation of about 3%. Above 500 eV a systematic decrease as a function of the neutron energy is observed. The same conclusions can be drawn by studying the ratio of the capture kernels as a function of the neutron energy.

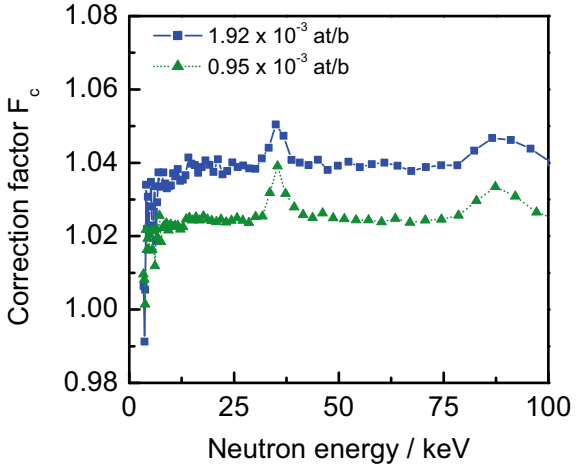

Fig. 10. Correction factor F_c to account for self-shielding and multiple interaction events as a function of the neutron energy. The factor is shown for the two sample geometries discussed in sect. 2.2 and specified in table 1.

From the results of a simultaneous analysis of the capture and transmission data one concludes that the capture data obtained in this work are fully consistent with the transmission data of Olsen *et al.* [3,4] and below 500 eV also with the parameters of Derrien *et al.* [8]. Unfortunately the transmission data of Harvey *et al.* [9] are only recommended for energies ≥ 1500 eV. Therefore, they cannot be used to clarify the difference for energies > 500 eV. Hence, new transmission measurements with a focus on the energy region between 500 eV and 2000 eV should be performed.

4.2 Energy region between 3.5 keV and 90 keV

4.2.1 Experimental $\overline{\sigma}_\gamma$ data obtained at GELINA

The relation between the average capture cross section $\overline{\sigma}_\gamma$ and average experimental yield $\overline{Y}_{exp}$, expressing the probability that a neutron creates a capture event in the sample, is mostly expressed as [30]:

$$\overline{Y}_{exp} = F_c\, n\, \overline{\sigma}_\gamma, \tag{8}$$

where n is the areal number density and F_c is an energy-dependent factor to correct for self-shielding and multiple interaction events, *i.e.* neutron scattering followed by neutron capture. This factor was calculated by Monte Carlo simulations using the MCNP 4C2 code [40] applying probability tables to produce resonance structured cross sections in the URR. These tables were created by NJOY [70] employing the average parameters discussed in sect. 4.2.3. The correction factor for the two sample geometries are compared in fig. 10. The structures at 35 keV and 90 keV are due to the presence of the aluminium foil around the sample. For relatively thin samples, as those used in this work, the uncertainty on this correction factor is $\leq 0.5\%$, as demonstrated in ref. [31].

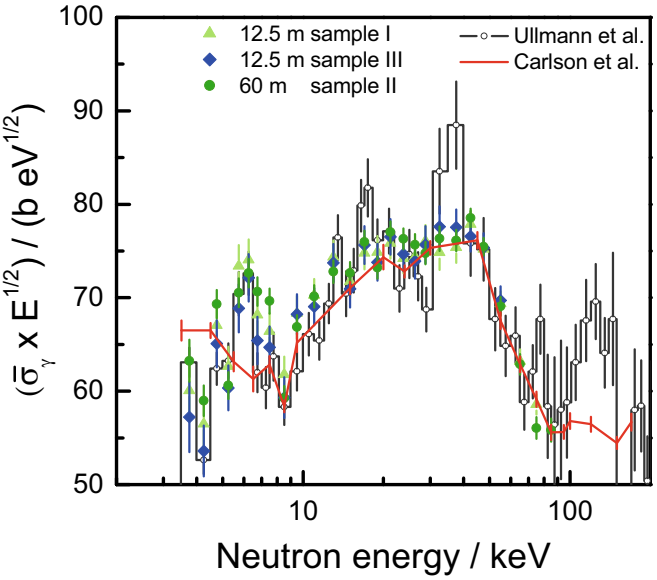

Fig. 11. Average capture cross section $\overline{\sigma}_\gamma$ for ^{238}U(n, γ) as a function of the neutron energy in the URR. The results derived from the capture measurements at a 12.5 m and 60 m station of GELINA using the samples specified in table 1 are compared with the results of Ullmann *et al.* [26] and the $\overline{\sigma}_\gamma$ recommended by Carlson *et al.* [19].

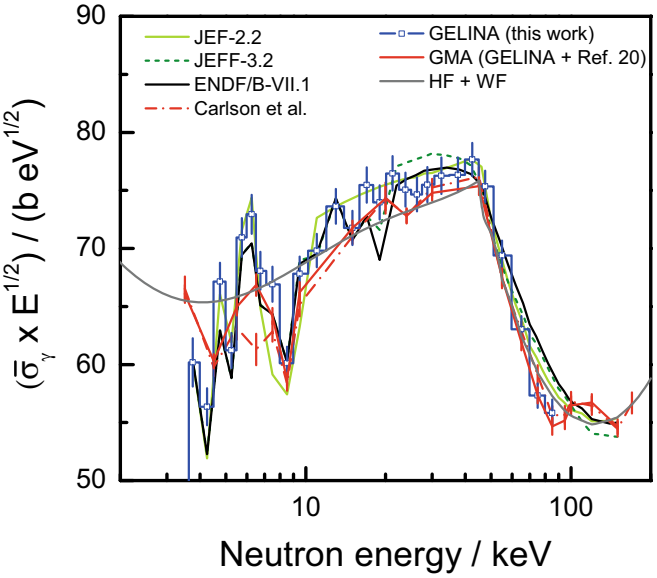

Fig. 12. Average capture cross section $\overline{\sigma}_\gamma$ for ^{238}U(n, γ) as a function of neutron energy in the URR. The results derived from a LSQ to the data obtained in this work together with the data specified in ref. [23] are compared with the results of Carlson *et al.* [19].The cross sections recommended in JEF-2.2, JEFF-3.2 and ENDF/B-VII.1 and the one resulting from a parameterisation of the data in table 2 in terms of average resonance parameters are also shown. The latter are indicated by HF+WF.

The average capture cross section data derived from the measurements with the three different sample configurations are shown in fig. 11. They are fully consistent considering only the uncertainties due to counting statistics and background subtraction. They are compared with the cross section recommended by Carlson *et al.* [19] and the one obtained by by Ullmann *et al.* [26]. The results in fig. 11 illustrate that for energies above 10 keV the results obtained in this work are in good agreement with the cross section recommended by Carlson *et al.* [19]. Deviations of more than 10% can be observed when comparing the $\overline{\sigma}_\gamma$ reported by Ullmann *et al.* [26] with the one of Carlson *et al.* [19]. Below 10 keV the data obtained in this work show a global resonance structure which is not present in the cross section of Carlson *et al.* [19]. This is due to the limited number of high-accuracy data resulting from TOF-measurements that are included in the data base [19, 23] and to the large energy bin widths used in the analysis of ref. [19]. The structure below 10 keV, which is observed in both the 12.5 m and 60 m data and in the data of Ullmann *et al.* [26], is most probably due to presence of a cluster of resonances as already suggested by Perez *et al.* [71].

From the GELINA data in fig. 11 an average capture cross section for energies between 3.5 keV and 90 keV was derived. The analysis included the correlated uncertainty due to the normalization factor, areal density and background correction on the capture response. The uncertainty on the normalization factor and the areal density was combined into one component with an uncertainty of 1.5%. The resulting $\overline{\sigma}_\gamma$ together with its uncertainty components are reported in table 2 and plotted in fig. 12. This figure includes the $\overline{\sigma}_\gamma$ of Carlson *et al.* [19] and the cross sections recommended in evaluated data libraries, *i.e.* those from independent evaluations in JEF-2.2, JEFF-3.2 and ENDF/B-VII.1. Figure 12 reveals differences $\geq 2.0\%$ between the recommended cross sections and the one of Carlson *et al.* [19].

For energies between 10 keV and 90 keV, the averaged capture cross section data in table 2 are on average about 0.7% higher compared to those of Carlson *et al.* [19], with a standard deviation of about 1.8%. The differences are within the 1.5% normalisation uncertainty and the uncertainties quoted by Carlson *et al.* [19]. The $\overline{\sigma}_\gamma$ obtained in this work is in very good agreement with the cross section recommended in JEF-2.2. The latter is based on the analysis of Moxon *et al.* [2] in the RRR and the one of Fröhner [14,15] in the URR. The separation between RRR and URR in this evaluation is at 10 keV.

The data obtained in this work can also be compared with the result of Wallner *et al.* [72]. For a neutron beam with a distribution that is very similar to a Maxwell-Boltzman distribution of $kT \sim 25.3$ keV they derived a spectrum averaged ^{238}U(n, γ) cross section of (391 ± 17) mb [72]. The latter was obtained from a combination of activation measurements and atom counting of the reaction products using accelerator mass spectrometry. This value was compared with an average value derived from a ^{238}U(n, γ) cross section that was constructed from the resonance parameters in appendix A for energies ≤ 1.2 keV, the average capture cross in table 2 for energies between 3.5 keV and 90 keV and the capture cross

Table 2. Average capture cross section ($\overline{\sigma}_\gamma$) and covariance data derived from the capture experiments reported in this work. The information to derive the full covariance matrix based on the AGS concept (eq. (7)) is given: the diagonal elements of the uncorrelated components u_u are in column 4, whereas columns 5–7 represent the matrix $S_{\boldsymbol{\eta}} = \{N, k_c, k_\varphi\}$. The uncertainty due to k_φ in eq. (4) can be neglected. A high precision is given to ensure that the resulting covariance matrix can be inverted.

E_l/eV	E_h/eV	$\overline{\sigma}_\gamma$/b	AGS			
			u_u/b	S_{N_c}/b	S_{k_c}/b	S_{k_φ}/b
3500	4000	0.9828 ± 0.0340	0.0138	0.0147	−0.0273	-1.7×10^{-5}
4000	4500	0.8645 ± 0.0246	0.0092	0.0130	−0.0188	-1.3×10^{-5}
4500	5000	0.9743 ± 0.0234	0.0085	0.0146	−0.0162	-1.2×10^{-5}
5000	5500	0.8448 ± 0.0209	0.0080	0.0127	−0.0146	-1.1×10^{-5}
5500	6000	0.9355 ± 0.0220	0.0088	0.0140	−0.0145	-1.1×10^{-5}
6000	6500	0.9226 ± 0.0212	0.0087	0.0138	−0.0135	-1.1×10^{-5}
6500	7000	0.8286 ± 0.0198	0.0085	0.0124	−0.0129	-1.1×10^{-5}
7000	8000	0.7726 ± 0.0174	0.0058	0.0116	−0.0116	-1.0×10^{-5}
8000	9000	0.6521 ± 0.0153	0.0056	0.0098	−0.0104	-9.7×10^{-6}
9000	10000	0.6958 ± 0.0152	0.0054	0.0104	−0.0096	-9.4×10^{-6}
10000	12000	0.6657 ± 0.0138	0.0039	0.0100	−0.0087	-9.1×10^{-6}
12000	14000	0.6458 ± 0.0132	0.0040	0.0097	−0.0079	-9.1×10^{-6}
14000	16000	0.5860 ± 0.0120	0.0040	0.0088	−0.0071	-8.9×10^{-6}
16000	18000	0.5787 ± 0.0117	0.0040	0.0087	−0.0067	-8.8×10^{-6}
18000	20000	0.5366 ± 0.0108	0.0039	0.0081	−0.0060	-8.5×10^{-6}
20000	22500	0.5246 ± 0.0103	0.0035	0.0079	−0.0056	-8.5×10^{-6}
22500	25000	0.4871 ± 0.0095	0.0033	0.0073	−0.0050	-8.2×10^{-6}
25000	27500	0.4608 ± 0.0090	0.0033	0.0069	−0.0048	-7.5×10^{-6}
27500	30000	0.4453 ± 0.0089	0.0035	0.0067	−0.0047	-7.1×10^{-6}
30000	35000	0.4230 ± 0.0088	0.0031	0.0064	−0.0052	-7.8×10^{-6}
35000	40000	0.3942 ± 0.0077	0.0026	0.0059	−0.0042	-7.2×10^{-6}
40000	45000	0.3767 ± 0.0069	0.0022	0.0057	−0.0033	-7.4×10^{-6}
45000	50000	0.3457 ± 0.0063	0.0021	0.0052	−0.0029	-8.2×10^{-6}
50000	60000	0.2959 ± 0.0055	0.0016	0.0044	−0.0028	-1.1×10^{-5}
60000	70000	0.2473 ± 0.0044	0.0013	0.0037	−0.0021	-1.6×10^{-5}
70000	80000	0.2093 ± 0.0038	0.0012	0.0031	−0.0018	-9.2×10^{-5}
80000	90000	0.1915 ± 0.0040	0.0017	0.0029	−0.0022	-1.4×10^{-4}

section from ENDF/B-VII.1 in the other energy regions. It should be noted that the energy region between 3.5 keV and 90 keV contributes for 90% to the spectrum averaged cross section. The resulting spectrum averaged cross section (407 ± 10) mb is within the quoted uncertainties in agreement with the one of Wallner *et al.* [72]. To derive the spectrum averaged cross section a correction factor of 1.04 [73] was used to transform the average cross section based on a pure Maxwell-Boltzman distribution to the real spectrum in the experiments of Wallner *et al.* [72].

4.2.2 Parameterisation of the $\overline{\sigma}_\gamma$ data obtained at GELINA

In the URR average cross sections can be parameterised by means of the Hauser-Feshbach statistical reaction theory with width - fluctuations (HF + WF), following various schemes for the fluctuation correction factor [74–78]. After taking into account the direct reactions, the average compound capture cross section in the URR can be expressed as a function of neutron strength functions and capture transmission coefficients [76]. For a statically well-deformed actinide nucleus such as ^{238}U direct reactions are important. In addition, direct reaction effects have an impact on the calculated compound elastic and inelastic cross sections.

The generalised ENDF-6 model together with the standard boundary conditions was used to parameterise the cross section data in table 2 in terms of average parameters. More details on the applied method can be found in refs. [31, 79, 80].

The transmission coefficient for a capture channel $T_\gamma^{J^\pi}$ was parameterised by [79]:

$$T_\gamma^{J^\pi}(E) = T_{\gamma,0}^{J^\pi} W_{T\gamma}^{J^\pi}(E), \tag{9}$$

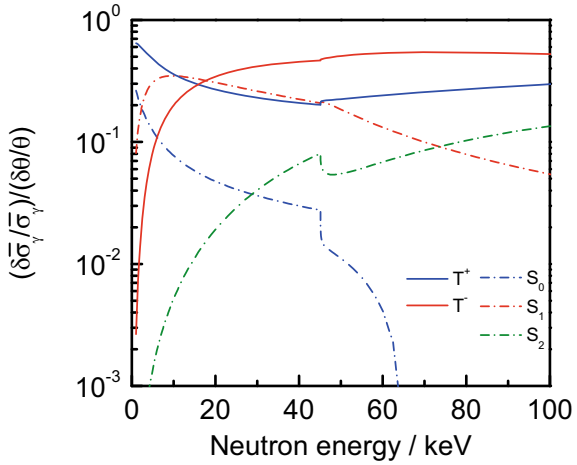

Fig. 13. Sensitivity $(\delta\overline{\sigma}_\gamma/\overline{\sigma}_\gamma)/(\delta\theta/\theta)$ of the average capture cross section for ^{238}U(n, γ) to the parameter θ as a function of neutron energy. The parameter θ represents the neutron strength functions $S_{\ell=0,1,2}$ and γ-ray transmission coefficients $T_{\gamma,0}^{1/2^+}$ and $T_{\gamma,0}^{1/2^-}$.

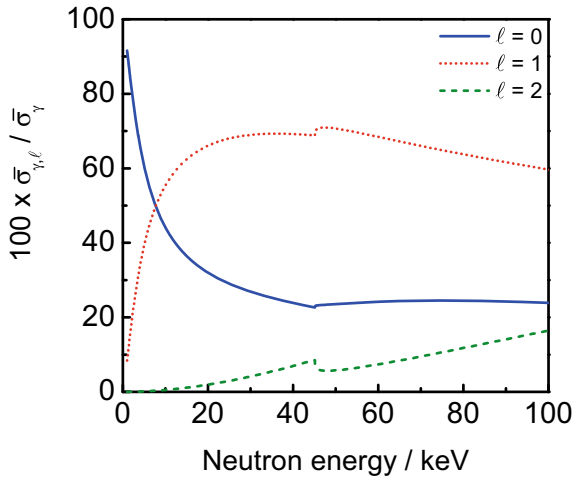

Fig. 14. Relative contribution of s-, p- and d-wave neutrons (ℓ = 0, 1 and 2) to the average capture cross section $\overline{\sigma}_\gamma$ for ^{238}U(n, γ) as a function of the neutron energy.

where $T_{\gamma,0}^{J^\pi} = T_\gamma^{J^\pi}(E=0)$ is the capture transmission coefficient at zero neutron energy. The energy dependence $W_{T\gamma}^{J^\pi}(E)$ can be approximated from the $T_\gamma^{J^\pi}(E)$ definition as a sum of single-channel photon transmission coefficients. The summation (integration) is over the transition types, multipolarities and photon energies of the primary γ-rays that de-excite the compound nucleus to lower-lying states of a given density. The J-dependence of $T_\gamma^{J^\pi}$ is usually determined from the J-dependence of the level density with the common assumption that the effective radiation widths only depend on the parity.

The sensitivities of the capture cross section for ^{238}U to the strength functions $S_{\ell=0,1,2}$ and capture transmission coefficients $T_{\gamma,0}^{1/2^+}$ and $T_{\gamma,0}^{1/2^-}$ for s- and p-waves, respectively, as a function of the neutron energy are shown in fig. 13. This figure shows that the $\overline{\sigma}_\gamma$ for ^{238}U in the energy region between 3.5 keV and 100 keV is mainly sensitive to capture transmission coefficients $T_{\gamma,0}^{1/2^+}$ and $T_{\gamma,0}^{1/2^-}$ and to the neutron strength function S_1 for p-waves. The decreasing sensitivity to the s-wave strength function and increasing sensitivity to the p-wave parameters with increasing energy follows from fig. 14, which gives the relative contribution of the partial waves to the average capture cross section.

The neutron strength functions $S_{\ell=0,1,2}$ and hard sphere scattering radius were adjusted to reproduce results of optical model calculations using the DCCOM potential of Quesada *et al.* [81]. The DCCOM smooth and weak energy dependence of calculated strength functions at energies below 150 keV was approximated by polynomials. The coupled-channel OPTMAN code [82,83] incorporated into the EMPIRE system [84] was used for the optical model calculations. The direct reaction contribution to the inelastic scattering was calculated by using the Dispersive Coupled-Channel Optical Model (DCCOM) potential of Quesada *et al.* [81]. The inelastic neutron scattering data of Capote *et al.* [85], which include compound-direct interference effects, were adopted for the present evaluation by modifying the calculated inelastic cross section. The resulting scattering radius $R = 9.483$ fm at zero energy is fully consistent with the effective scattering radius used for the analysis in the RRR.

The capture transmission coefficients for s-waves $T_{\gamma,0}^{1/2^+}$ and p-waves $T_{\gamma,0}^{1/2^-}$ were derived from a least squares adjustment to the $\overline{\sigma}_\gamma$ cross section data in table 2. The capture channel transmission coefficients for d-wave neutrons were determined from the s-wave coefficient. To avoid bias effects due to Peelle's Pertinent Puzzle [86], the uncertainties resulting from the normalization of the capture data were based on the parameterised cross section [87]. The resulting parameters are listed in table 3

Table 3. Average parameters ($S_{\ell=0,1,2}$, $T_{\gamma,0}^{1/2^+}$, $T_{\gamma,0}^{1/2^-}$) and scattering radius R at zero neutron energy. The scattering radius R and neutron strength functions $S_{\ell=0,1,2}$ were derived from optical model calculations using the DCCOM potential of Quesada *et al.* [81]. The capture transmission coefficients were derived from a LSQ fit to the data in table 2 together with the cross section of Carlson *et al.* [19]. The uncertainties on the parameters and correlation coefficient $\rho(T_{\gamma,0}^{1/2^+}, T_{\gamma,0}^{1/2^-})$ were derived by propagating a full correlated 1.5% normalisation uncertainty on the data.

	θ	$\rho(\theta,\theta')$	
R/fm	9.483		
S_0 / 10^{-4}	1.064		
S_1 / 10^{-5}	1.641		
S_2 / 10^{-4}	1.376		
$T_{\gamma,0}^{1/2^+}$ / 10^{-3}	6.28 ± 0.15	1.000	0.655
$T_{\gamma,0}^{1/2^-}$ / 10^{-3}	6.80 ± 0.12	0.655	1.000

Table 4. Average capture cross section ($\overline{\sigma}_\gamma$), its uncertainty $u_{\overline{\sigma}_\gamma}$ and correlation coefficient $\rho(\overline{\sigma}_{\gamma,i}, \overline{\sigma}_{\gamma,j})$ derived from a LSQ analysis of the capture data reported in this work together with the data reported in ref. [23]. Above 20 keV the LSQ analysis is based on point wise data.

E/ eV	$\overline{\sigma}_\gamma$/b	$\rho(\overline{\sigma}_{\gamma,i}, \overline{\sigma}_{\gamma,j}) \times 100$															
3000–4000	1.1170 ± 0.0160	100	27	20	19	20	17	22	24	19	23	21	24	20	20	19	16
4000–5000	0.8987 ± 0.0096		100	34	24	26	23	29	34	27	32	30	35	28	29	28	24
5000–6000	0.8761 ± 0.0100			100	30	19	22	30	33	28	33	31	36	29	30	29	24
6000–7000	0.8291 ± 0.0104				100	31	19	29	32	28	32	31	36	29	30	29	24
7000–8000	0.7410 ± 0.0085					100	29	27	31	25	30	28	32	26	27	26	22
8000–9000	0.6368 ± 0.0062						100	29	33	24	31	29	31	25	26	25	21
9000–10000	0.6796 ± 0.0069							100	39	34	39	37	42	35	36	34	29
10000–20000	0.5859 ± 0.0044								100	39	48	45	50	40	42	39	34
20000	0.5254 ± 0.0053									100	42	38	44	37	38	36	31
24000	0.4700 ± 0.0035										100	51	53	43	44	42	37
30000	0.4318 ± 0.0035											100	53	43	45	42	37
45000	0.3553 ± 0.0028												100	51	49	47	41
55000	0.2879 ± 0.0027													100	49	37	35
65000	0.2429 ± 0.0022														100	51	33
75000	0.2094 ± 0.0020															100	48
85000	0.1875 ± 0.0020																100

and the calculated cross section, referred to as HF+WF, is shown in fig. 12.

The covariance on the parameters include the propagation of a full correlated 1.5% normalisation uncertainty on the data. However, it is based on a propagation without considering uncertainties on the neutron strength functions. Hence, the uncertainty on the average capture cross section derived from the data in table 3 will be underestimated. A final evaluation of the parameters including a full covariance matrix requires an analysis that includes experimental total cross section data in the URR.

4.2.3 Least squares analysis of $\overline{\sigma}_\gamma$ data

The experimental capture cross section derived from the measurements reported in this work were included in a least squares adjustment (LSQ) together with the data listed in ref. [23]. For this analysis the GMA code of Poenitz [20] was used. The resulting $\overline{\sigma}_\gamma$ is listed in table 4 and compared in fig. 12 with the one of Carlson *et al.* [19]. The effect of including the GELINA data produces a $\overline{\sigma}_\gamma$ that reproduces better the structure in the region around 6 keV and is on average about 0.5% higher in the energy region above 10 keV. It also reduces the uncertainty by about 25%.

5 Summary and conclusions

Capture cross section measurements were performed at a 12.5 m and 60 m capture measurement station of the GELINA time-of-flight facility using samples with different characteristics. The uncertainty related to the normalization and weighting function was about 1.5%. Full covariance data were produced by propagating both uncorrelated and correlated uncertainty components.

The capture yield obtained at GELINA and the transmission data of Olsen *et al.* [3,4] were used in a simultaneous resonance shape analysis to derive resonance parameters for neutron-induced reactions on ^{238}U in the energy region below 1.2 keV. The contribution of bound states was adjusted to produce a parameter file that is fully consistent with the capture data obtained in this work and the transmission data of Olsen *et al.* [3, 4], without the need of any additional background or normalization correction. The neutron widths in the region below 500 eV are in very good agreement with those reported by Derrien *et al.* [8]. They are are on average about 0.4% higher with a standard deviation of about 3%. For resonance energies above 500 eV a larger systematic difference is observed. The neutron widths are systematically lower with a difference that increases with increasing resonance energy. The average radiation width of 22.5 meV is about 2.2% lower compared to the one derived by Derrien *et al.* [8].

Average capture cross section data were derived for neutron energies between 3.5 keV and 90 keV. Below 10 keV the data obtained in this work show a structure that confirms the presence of a resonance cluster. Above 10 keV, they deviate on average by less than 1% from the average cross section that was derived from a least squares adjustment to the experimental data which were available in the literature prior to this work. This deviation is within the quoted uncertainties. The average cross section data

Table 5. Resonance parameters (E_r, J^π, $g\Gamma_n$, Γ_γ, Γ_f) for the neutron-induced reaction on ^{238}U below 1200 eV.

E_r/eV	J^π	$g\Gamma_n$/meV	Γ_γ/meV	$\rho(\Gamma_n, \Gamma_\gamma)$	Γ_f/μeV
−33.300	0.5^+	4.808	23.0		
−3.500	0.5^+	0.049	26.1		
6.674	0.5^+	1.4923 ± 0.0011	22.711 ± 0.019	−0.77	0.00988 ± 0.00039
10.240	1.5^-	$(1.698 \pm 0.010) \times 10^{-3}$			
19.525	1.5^-	$(1.570 \pm 0.021) \times 10^{-3}$			
20.872	0.5^+	10.076 ± 0.010	22.753 ± 0.024		0.0546 ± 0.0011
36.683	0.5^+	33.592 ± 0.020	22.264 ± 0.024	−0.47	0.00972 ± 0.00059
63.523	0.5^-	$(1.049 \pm 0.021) \times 10^{-2}$			
66.030	0.5^+	24.275 ± 0.031	22.415 ± 0.043	−0.40	0.0519 ± 0.0022
80.752	0.5^+	1.8559 ± 0.0041			0.0595 ± 0.0013
83.711	0.5^-	$(1.081 \pm 0.039) \times 10^{-2}$			
89.249	0.5^-	0.1038 ± 0.0012			
102.563	0.5^+	70.871 ± 0.080	23.173 ± 0.040	−0.26	0.0129 ± 0.0026
116.904	0.5^+	25.270 ± 0.071	21.445 ± 0.062	−0.18	
145.666	0.5^+	0.9306 ± 0.0035			
152.458	1.5^-	$(5.820 \pm 0.150) \times 10^{-2}$			
165.297	0.5^+	3.435 ± 0.010			
173.226	0.5^-	$(5.280 \pm 0.160) \times 10^{-2}$			
189.675	0.5^+	170.82 ± 0.21	21.368 ± 0.044	−0.13	0.0356 ± 0.0067
194.809	1.5^-	$(1.230 \pm 0.310) \times 10^{-2}$			
208.523	0.5^+	50.39 ± 0.14	22.280 ± 0.060	−0.01	0.0820 ± 0.0095
214.907	1.5^-	$(6.170 \pm 0.300) \times 10^{-2}$			
237.399	0.5^+	26.71 ± 0.11	23.749 ± 0.098	−0.35	0.035 ± 0.010
242.762	0.5^-	0.2033 ± 0.0040			
253.932	1.5^-	0.1070 ± 0.0035			
263.970	1.5^-	0.2867 ± 0.0042			
273.670	0.5^+	25.15 ± 0.14	21.98 ± 0.11	−0.46	
275.193	1.5^-	0.2039 ± 0.0069			
282.471	1.5^-	0.1115 ± 0.0041			
291.003	0.5^+	16.56 ± 0.11	22.62 ± 0.19	−0.73	
311.318	0.5^+	1.0574 ± 0.0085			
347.810	0.5^+	80.00 ± 0.28	21.098 ± 0.067	0.09	0.230 ± 0.018
351.893	1.5^-	0.2050 ± 0.0076			
376.936	0.5^+	1.129 ± 0.011			0.14 ± 0.14
397.624	0.5^+	6.227 ± 0.039			
410.260	0.5^+	19.14 ± 0.17	25.34 ± 0.33	−0.80	
434.087	0.5^+	10.089 ± 0.053			
439.761	1.5^-	0.282 ± 0.010			
454.109	0.5^-	0.425 ± 0.010			
463.175	0.5^+	5.701 ± 0.034			1.32 ± 0.12
478.433	0.5^+	4.135 ± 0.027			0.224 ± 0.130
488.852	0.5^-	0.874 ± 0.013			
518.385	0.5^+	48.80 ± 0.30	22.54 ± 0.10	−0.17	0.231 ± 0.035
523.341	0.5^-	0.305 ± 0.013			
535.302	0.5^+	43.82 ± 0.30	23.38 ± 0.12	−0.32	0.369 ± 0.040
542.458	1.5^-	0.118 ± 0.016			
556.128	1.5^-	0.710 ± 0.060			

Table 5. Continued.

E_r/eV	J^π	$g\Gamma_n$/meV	Γ_γ/meV	$\rho(\Gamma_n, \Gamma_\gamma)$	Γ_f/μeV
556.791	1.5^-	0.192 ± 0.043			
580.126	0.5^+	38.54 ± 0.30	24.59 ± 0.15	-0.45	
595.069	0.5^+	86.50 ± 0.44	22.41 ± 0.10	0.03	1.004 ± 0.051
606.724	0.5^-	0.270 ± 0.017			
619.989	0.5^+	28.43 ± 0.30	23.68 ± 0.23	-0.62	0.150 ± 0.041
624.186	1.5^-	0.760 ± 0.021			
628.535	0.5^+	6.408 ± 0.052			
661.189	0.5^+	126.41 ± 0.57	23.19 ± 0.10	0.09	
668.425	1.5^-	0.168 ± 0.20			
677.718	0.5^-	0.652 ± 0.22			
693.043	0.5^+	39.54 ± 0.40	23.07 ± 0.17	0.60	
698.010	1.5^-	0.281 ± 0.020			
708.266	0.5^-	19.38 ± 0.30	25.70 ± 0.51	0.83	37.9 ± 1.1
710.459	1.5^-	1.184 ± 0.040			
721.558	0.5^-	1.494 ± 0.045			1854 ± 235
730.023	0.5^-	1.005 ± 0.030			148.9 ± 7.2
732.423	0.5^-	2.040 ± 0.038			
743.091	0.5^-	0.377 ± 0.023			
756.211	1.5^-	0.527 ± 0.024			
765.012	0.5^+	8.215 ± 0.086			9.01 ± 0.76
779.246	1.5^-	2.035 ± 0.035			
790.747	0.5^+	6.696 ± 0.069			
792.135	1.5^-	0.150 ± 0.027			
808.138	0.5^-	0.533 ± 0.043			
821.498	0.5^+	64.88 ± 0.54	21.31 ± 0.13	-0.15	0.24 ± 0.14
823.359	0.5^-	0.4354 ± 0.0063			
828.592	1.5^-	0.242 ± 0.025			
846.545	0.5^-	0.6620 ± 0.030			
851.067	0.5^+	60.41 ± 0.62	23.27 ± 0.19	-0.22	2.64 ± 0.28
856.166	0.5^+	86.63 ± 0.66	23.15 ± 0.17	-0.12	1.41 ± 0.18
866.461	0.5^+	5.672 ± 0.071			
891.086	1.5^-	0.614 ± 0.031			
905.095	0.5^+	51.51 ± 0.57	22.98 ± 0.19	-0.34	
909.788	1.5^-	1.310 ± 0.045			
925.147	0.5^+	14.60 ± 0.15			
937.063	0.5^+	148.56 ± 0.87	21.56 ± 0.13	0.12	
958.560	0.5^+	203.7 ± 1.0	21.46 ± 0.13	0.16	
977.383	0.5^-	0.714 ± 0.037			
984.219	1.5^-	0.197 ± 0.044			
991.616	0.5^+	378.1 ± 1.4	23.78 ± 0.13	0.07	
1011.329	1.5^-	1.695 ± 0.052			
1022.956	0.5^+	8.39 ± 0.12			
1029.011	0.5^-	2.256 ± 0.063			
1033.489	1.5^-	0.677 ± 0.046			
1054.470	0.5^+	90.07 ± 0.82	22.52 ± 0.16	-0.08	
1062.585	1.5^-	0.848 ± 0.050			
1067.483	0.5^-	1.184 ± 0.053			
1073.936	1.5^-	0.779 ± 0.048			

Table 5. Continued.

E_r/eV	J^π	$g\Gamma_n$/meV	Γ_γ/meV	$\rho(\Gamma_n, \Gamma_\gamma)$	Γ_f/μeV
1081.605	1.5^-	1.490 ± 0.054			
1094.908	0.5^-	1.751 ± 0.076			
1098.271	1.5^-	2.76 ± 0.35			
1098.706	0.5^+	16.99 ± 0.67	24.22 ± 0.96	-0.85	
1102.631	1.5^-	1.874 ± 0.073			
1109.092	0.5^+	31.17 ± 0.63	25.12 ± 0.46	-0.71	
1118.998	1.5^-	0.618 ± 0.075			
1131.146	1.5^-	3.256 ± 0.067			
1140.338	0.5^+	229.2 ± 1.3	21.31 ± 0.10	0.02	2.33 ± 0.26
1154.869	1.5^-	0.82 ± 0.10			
1158.884	0.5^-	0.444 ± 0.080			
1167.597	0.5^+	85.44 ± 0.94	22.43 ± 0.19	-0.12	15.55 ± 0.76
1177.213	0.5^+	61.04 ± 0.80	24.02 ± 0.27	-0.36	
1194.814	0.5^+	89.19 ± 0.91	23.42 ± 0.19	-0.13	
1211.058	0.5^+	10.05 ± 0.32	19.90 ± 1.30	-0.81	301.2 ± 6.0

were used to derive average capture transmission coefficients for s- and p-waves, *i.e.* $T_{\gamma,0}^{1/2^+}$ and $T_{\gamma,0}^{1/2^-}$, together with their covariance matrix. They were also included in a least squares analysis to derive an average capture cross section in the URR based on experimental data reported in the literature.

We are grateful to the GELINA operators for the dedicated and skillful running of the accelerator and to the Nuclear Data Section of the IAEA for their interest in this work. This work was supported by the European Commission through the projects ANDES (contract FP7-249671) and the CIELO project coordinated by the Nuclear Energy Agency of the OECD. It was also supported by a grant from the KAERI Initiative Program.

Appendix A.

Table 5 lists the resonance parameters, *i.e.* resonance energy E_r, spin and parity J^π, neutron width multiplied by the statistical factor $g\Gamma_n$, radiation width Γ_γ and fission width Γ_f, for the neutron-induced reaction on ^{238}U below 1200 eV. The parameters (E_r, $g\Gamma_n$, Γ_γ) were derived from a simultaneous fit to the GELINA capture reported in this work and ORLEA transmission data of refs. [3,4]. The correlation coefficient $\rho(\Gamma_n, \Gamma_\gamma)$ is given when both Γ_γ and Γ_n were fitted. The uncertainties on the resonance energy resulting from the fit are smaller compared to the one due to the original uncertainty on the resonance energies used to determine the flight path length. The parameters of negative resonances that were changed with respect to ENDF/B-VII.1 (resonances at -7 eV and -33 eV in ENDF/B-VII.1) are also given. The fission width were adjutested to reproduce the fission kernels (see eq. (1)) reported by Difilippo *et al.* [7]. The uncertainties on the fission widths are dominated by the uncertainty on the fission kernels. *Please note that the quoted uncertainties were obtained by only propagating uncorrelated uncertainties due to counting statistics.*

References

1. M.B. Chadwick, E. Dupont *et al.*, Nucl. Data Sheets **118**, 1 (2014).
2. M.C. Moxon, M.G. Sowerby, J.B. Brisland, *^{238}U Resolved Resonance Parameters*, in *Proceedings of the International Conference on Physics of Reactors, Operation, Design and Computation, PHYSOR'90 Marseille, 23–27 April 1990* (1990) pp. III 41–51.
3. D.K. Olsen, G. de Saussure, R.B. Perez, E.G. Silver, F.C. Difilippo, R.W. Ingle, H. Weaver, Nucl. Sci Eng. **62**, 479 (1977).
4. D.K. Olsen, G. de Saussure, R.B. Perez, F.C. Difilippo, R.W. Ingle, Nucl. Sci. Eng. **66**, 141 (1978).
5. G. de Saussure, E.G. Silver, R.B. Perez, R. Ingle, H. Weaver, Nucl. Sci. Eng. **51**, 385 (1973).
6. R.L. Macklin, R.B. Perez, G. de Saussure, R.W. Ingle, Ann. Nucl. Energy **18**, 567 (1991).
7. F.C. Difilippo, R.B. Perez, G. de Saussure, D.K. Olsen, R.W. Ingle, Phys. Rev. C **21**, 1400 (1980).
8. H. Derrien, L.C. Leal, N.M. Larson, A. Courcelle, *Neutron Resonance Parameters and Calculated Cross Sections from Reich-Moore Analysis of Experimental Data in the Neutron Energy Range from 0 to 20 keV*, ORNL/TM-2005/241, Oak Ridge National Laboratory (2005).
9. J.A. Harvey, N.W. Hill, F.G. Perey, G.L. Tweed, L. Leal, *High-Resolution Neutron Transmission Measurements on ^{235}U, ^{239}Pu, and ^{238}U*, in *Proceedings of the International Conference on Nuclear Data for Science and Technology, Mito, Japan, 30 May–3 June, 1988* (1988) pp. 115–118.
10. F. Corvi, F. Fioni, *Shape of the ^{238}U Neutron Capture Cross Section in the Range 0.002–0.1 eV*, in *Proceedings of the International Conference on Nuclear Data for Science and Technology, Mito, Japan, 30 May–3 June, 1988* (1988) pp. 127–130.

11. A. Meister *et al.*, *Experimental Study of the Doppler Broadening of Neutron Resonances at GELINA*, in *Proceedings of the International Conference on Nuclear Data for Science and Technology (NDST-97), Trieste, Italy, 19-24 May, 1997* (1997) pp. 435–439.
12. F. Gunsing, K. Athanassopulos, F. Corvi, H. Postma, Yu. P. Popov, E.I. Sharapov, Phys. Rev. C **56**, 1266 (1997).
13. A. Trkov, G.L. Molnár, Zs. Révay, S.F. Mughabghab, R.B. Firestone, V.G. Pronyaev, A.L. Nichols, M.C. Moxon, Nucl. Sci. Eng. **150**, 336 (2005).
14. F.H. Fröhner, Nucl. Sci. Eng. **103**, 119 (1989).
15. F.H. Fröhner, Nucl. Sci. Eng. **111**, 404 (1992).
16. V. M. Maslov, Yu. V. Porodzinskij, M. Baba, A. Hasegawa, Ann. Nucl. Energy **29**, 1707 (2002).
17. A. Courcelle, H. Derrien, L.C. Leal, N.M. Larson, Nucl. Sci. Eng. **156**, 391 (2007).
18. L.E. Kazakov, V.N. Kononov, G.N. Manturov, E.D. Poletaev, M.V. Bokhovko, V.M. Timokhov, A.A. Voevodskij, Yad. Konstant. **3**, 37 (1986) (in Russian), Translation in INDC(CCP)-319/L, September 1990.
19. A.D. Carlson, V.G. Pronyaev, D.L. Smith, N.M. Larson, Z. Chen, G.M. Hale, F.-J. Hambsch, E.V. Gai, Soo-Youl Oh, S.A. Badikov, T. Kawano, H. M. Hofman, H. Vonach, S. Tagesen, Nucl. Data Sheets **110**, 3215 (2009).
20. W.P. Poenitz, *Data Interpretation, Objective, Evaluation Procedures and Mathematical Technique for the Evaluation of Energy-Dependent Ratio, Shape and Cross Section Data*, in *Proceedings of the Conference on Nuclear Data Evaluation Methods and Procedures*, BNL-NCS-51363, p. 249 (1981).
21. `https://www-nds.iaea.org/standards/codes.html` (12/03/2016).
22. V.G. Pronyaev, A.D. Carlson, R. Capote Noy, *Current Status of Neutron Standards, Summary report of the Technical Meeting, IAEA Headquarters, Vienna, Austria, 1–5 December 2014*, INDC(NDS)-0677 (2015) `https://www-nds.iaea.org/publications/indc/indc-nds-0677.pdf` (15/03/2016).
23. S.A. Badikov, Chen Zhenpeng, A.D. Carlson, E.V. Gai, G.M. Hale, F.-J. Hambsch, H.M. Hofmann, T. Kawano, N.M. Larson, V.G. Pronyaev, D.L. Smith, Soo-Youl Oh, S. Tagesen, H. Vonach, IAEA Report, STI/PUB/1291, (2007).
24. Kopecky *et al.*, *Status of Evaluated Data Files for* ^{238}U *in the Resonance region*, JRC Technical Report, EUR 27504 EN (2015).
25. `http://www.oecd-nea.org/dbdata/hprl/` (15/03/2016).
26. J.L. Ullmann, T. Kawano, T.A. Bredeweg, A. Couture, R.C. Haight, M. Jandel, J.M. O'Donnell, R.S. Rundberg, D.J. Vieira, J.B. Wilehlmy, J.A. Becker, A. Chyzh, C.Y. Wu, B. Baramsai, G.E. Mitchell, M. Krtička, Phys. Rev. C **89**, 034603 (2014).
27. F. Mingrone, the n_TOF Collaboration, Nucl. Data Sheets **119**, 18 (2014).
28. T. Wright, the n_TOF Collaboration, Nucl. Data Sheets **119**, 26 (2104).
29. Project within the Seventh Framework Program of the European Commission, *Accurate Nuclear Data for nuclear Energy Sustainability*, ANDES (FP7-249671).
30. P. Schillebeeckx, B. Becker, Y. Danon, K. Guber, H. Harada, J. Heyse, A.R. Junghans, S. Kopecky, C. Massimi, M. Moxon, N. Otuka, I. Sirakov, K. Volev, Nucl. Data Sheets **113**, 3054 (2012).
31. C. Massimi, B. Becker, E. Dupont, S. Kopecky, C. Lampoudis, R. Massarczyk, M. Moxon, V. Pronyaev, P. Schillebeeckx, I. Sirakov, R. Wynants, Eur. Phys. J. A **50**, 124 (2014).
32. W. Mondelaers, P. Schillebeeckx, Not. Neutroni Luce Sincrotrone **11**, 19 (2006) `https://www.fisica.uniroma2.it/~notiziario/2006/` (03/05/2016).
33. D. Tronc, J.M. Salomé, K.H. Böckhoff, Nucl. Instrum. Methods A **228**, 217 (1985).
34. J.M. Salome, R. Cools, Nucl. Instrum. Methods **179**, 13 (1981).
35. C.R. Brun, Nucl. Instrum. Methods A **493**, 106 (2002).
36. R.L. Macklin, J.H. Gibbons, Phys. Rev. **159**, 1007 (1967).
37. A. Borella, G. Aerts, F. Gunsing, M. Moxon, P. Schillebeeckx, R. Wynants, Nucl. Instrum. Methods A **577**, 626 (2007).
38. P. Schillebeeckx, A. Borella, S. Kopecky, C. Lampoudis, C. Massimi, M. Moxon, J. Korean Phys. Soc. **59**, 1563 (2011).
39. M.C. Moxon, J.B. Brisland, *GEEL REFIT, A least squares fitting program for resonance analysis of neutron transmission and capture data computer code*, in AEA-InTec-0630, AEA Technology, October 1991.
40. J. Briemeister, *MCNP, A General Monte Carlo N-Particle Transport Code*, Version 4C2, in LA-13709-M (2000).
41. G. Giorginis, V. Khriatchkov, Nucl. Instrum. Methods A **538**, 550 (2005).
42. J. Gonzalez, C. Bastian, S. de Jonge, K. Hofmans, *Modular Multi-Parameter Multiplexer MMPM, Hardware description and user guide*, Internal Report GE/R/INF/06/97, IRMM, Geel (1997).
43. L.C. Mihailescu, A. Borella, C. Massimi, P. Schillebeeckx, Nucl. Instrum. Methods A **600**, 453 (2009).
44. `https://www.mitutoyo.co.jp/eng/` (03/05/2016).
45. A. Borella, K. Volev, A. Brusegan, P. Schillebeeckx, F. Corvi, N. Koyumdjieva, N. Janeva, A.A. Lukyanov, Nucl. Sci. Eng. **152**, 1 (2006).
46. O. Litaize, O. Serot, D. Regnier, C. Manailescu, Nucl. Data Sheets **118**, 216 (2014).
47. D.G. Madland, Nucl. Phys. A **772**, 113 (2006).
48. A. Oberstedt, P. Halipré, F.-J. Hambsch, M. Lebois, S. Oberstedt, J.N. Wilson, Phys. Proc. **64**, 91 (2015).
49. J. Fréhaut, *Neutron gamma competition in fast fission*, in *Proceedings of a Consultants Meeting on Physics of Neutron Emission in Fission, Mito, Japan, 24–27 May 1988* (1988) pp. 99–111, `https://www-nds.iaea.org/publications/` (03/05/2016).
50. N. Yamamuro, T. Hayase, T. Doi, Y. Fujita, K. Kobayashi, R.C. Block, Nucl. Instrum. Methods **133**, 531 (1976).
51. R.L. Macklin, J. Halperin, R.R. Winters, Nucl. Instrum. Methods **164**, 213 (1979).
52. G. Schramm, R. Massarczyk, A.R. Junghans *et al.*, Phys. Rev. C **85**, 014311 (2012).
53. R. Massarczyk, G. Schramm, A.R. Junghans, R. Schwengner, M. Anders, T. Belgya, R. Beyer, E. Birgersson, A. Ferrari, E. Grosse, R. Hannaske, Z. Kis, T. Kögler, K. Kosev, M. Marta, L. Szentmiklósi, A. Wagner, J.L. Weil, Phys. Rev. C **87**, 044306 (2013).
54. E. Browne, J.K. Tuli, Nucl. Data Sheets **114**, 293 (2014).
55. T. von Egidy, D. Bucurescu, Phys. Rev. C. **80**, 054310 (2009).
56. A.R. Junghans, G. Rusev, R. Schwengner, A. Wagner, E. Grosse, Phys. Lett. B **670**, 200 (2008).

57. K. Heyde, P. von Neumann-Cosel, A. Richter, Rev. Mod. Phys. **82**, 2365 (2010).
58. R. Capote, M. Herman, P. Obložinský, P.G. Young, S. Goriely, T. Belgya, A.V. Ignatyuk, A.J. Koning, S. Hilaire, V.A. Plujko, M. Avrigeanu, O. Bersillon, M.B. Chadwick, T. Fukahori, Zhigang Ge, Yinlu Han, S. Kailas, J. Kopecky, V.M. Maslov, G. Reffo, M. Sin, E.Sh. Soukhovitskii, P. Talou, Nucl. Data Sheets **110**, 3107 (2009).
59. C. Bastian, *General procedures and computational methods for generating covariance matrices*, in *Proceedings of the International Symposium on Nuclear Data Evaluation Methodology, 1992* (1992) pp. 642–649.
60. B. Becker, C. Bastian, F. Emiliani, F. Gunsing, J. Heyse, K. Kauwenberghs, S. Kopecky, C. Lampoudis, C. Massimi, N. Otuka, P. Schillebeeckx, I. Sirakov, J. Instrum. **7**, P11002 (2012).
61. N. Otuka, A. Borella, S. Kopecky, C. Lampoudis, P. Schillebeeckx, J. Korean Phys. Soc. **59**, 1314 (2011).
62. F. Gunsing, P. Schillebeeeckx, V. Semkova, *Summary Report of the Consultants' Meeting on EXFOR Data in Resonance Region and Spectrometer Response Function, IAEA Headquarters, Vienna, Austria, 8-10 October 2013*, INDC(NDS)-0647 (2013), `https://www-nds.iaea.org/index-meeting-crp/CM-RF-2013/` (03/05/2016).
63. C.W. Reich, M.S. Moore, Phys. Rev. **111**, 929 (1958).
64. A.M. Lane, R.G. Thomas, Rev. Mod. Phys. **30**, 257 (1958).
65. M. Flaska, A. Borella, D. Lathouwers, L.C. Mihailescu, W. Mondelaers, A.J.M. Plompen, H. van Dam, T.H.J.J. van der Hagen, Nucl. Instrum. Methods A **531**, 392 (2004).
66. D. Ene, C. Borcea, S. Kopecky, W. Mondelaers, A. Negret, A.J.M. Plompen, Nucl. Instrum. Methods A **618**, 54 (2010).
67. M. Moxon, private communication.
68. L. Koester, H. Rauch, E. Seymann, At. Data Nucl. Data Tables **49**, 65 (1991).
69. L.M. Bollinger, G.E. Thomas, Phys. Rev. **171**, 1293 (1963).
70. R.E. MacFarlane, A.C. Kahler, Nucl. Data Sheets **111**, 2739 (2010).
71. R.B. Perez, G. de Saussure, R.L. Macklin, J. Halperin, Phys. Rev. C **20**, 528 (1979).
72. A. Wallner, T. Belgya, M. Bichler, K. Buczak, F. Käppeler, C. Lederer, A. Mengoni, F. Quinto, P. Steier, L. Szentmiklosi, Phys. Rev. Lett. **112**, 192501 (2014).
73. A. Wallner, private communication (2016).
74. L. Dresner, *Proceedings of the International Conference on Neutron Reactions with the Nucleus, Columbia Univeristy, 1957*, Report CU-157 (1957) p. 71.
75. P.A. Moldauer, Nucl. Phys. A **344**, 185 (1980).
76. H.M. Hofman, J. Richert, J.W. Tepel, W.A. Weidenmuller, Nucl. Phys. A **344**, 402 (1975).
77. J.J.M. Verbaarschot, H.A. Weidenmüller, M.R. Zirnbauer, Phys. Rep. **129**, 367 (1985).
78. H. Henryson, B.J. Toppel, C.G. Sternberg, Argonne National Laboratory Report ANL-8144 (ENDF-239) (1976).
79. I. Sirakov, R. Capote, F. Gunsing, P. Schillebeeckx, A. Trkov, Ann. Nucl. Energy **35**, 1223 (2008).
80. I. Sirakov, B. Becker, R. Capote, E. Dupont, S. Kopecky, C. Massimi, P. Schillebeeckx, Eur. Phys. J. A **49**, 144 (2013).
81. J.M. Quesada, R. Capote, E.Sh. Soukhovitskii, S. Chiba, Nucl. Data Sheets **118**, 270 (2014).
82. E.Sh. Sukhovitskii, S. Chiba, O. Iwamoto, K. Shibata, T. Fukahori, G. Mororovskij, JAERI-Data/Code 2005-002 (Japan Atomic Energy Agency, 2005).
83. E.Sh. Soukhovitski, S. Chiba, R. Capote, J.M. Quesada, S. Kunieda, G. Mororovskij, JAERI-Data/Code 2008-025 (Japan Atomic Energy Agency, 2008).
84. M. Herman, R. Capote, B.V. Carlson, P. Obložinský, M. Sin, A. Trkov, H. Wienke, V. Zerkin, Nucl. Data Sheets **108**, 2655 (2007).
85. R. Capote, A. Trkov, M. Sin, M. Herman, A. Daskalakis, Y. Danon, Nucl. Data Sheets **118**, 26 (2014).
86. G. D'Agostini, Nucl. Instrum. Methods A **346**, 306 (1994).
87. B. Becker, R. Capote, S. Kopecky, C. Massimi, P. Schillebeeckx, I. Sirakov, K. Volev, Nucl. Data Sheets **118**, 381 (2014).